

New Clues About Light Sterile Neutrinos: Preference for Models with Damping Effects in Global Fits

J.M. Hardin,^{1,*} I Martinez-Soler,² A. Diaz,¹ M. Jin (靳淼辰),²
N.W. Kamp,¹ C.A. Argüelles,² J.M. Conrad,¹ and M.H. Shaevitz³

¹*Dept. of Physics, Massachusetts Institute of Technology, Cambridge, MA 02139, USA*

²*Dept. of Physics, Harvard University, Cambridge, MA 02138, USA*

³*Dept. of Physics, Columbia University, New York, NY, 10027, USA*

(Dated: November 14, 2022)

This article reports global fits of short-baseline neutrino data to oscillation models involving light sterile neutrinos. In the commonly-used 3+1 plane wave model, there is a well-known 4.9σ tension between data sets sensitive to appearance and disappearance of neutrinos. We find that models that damp the oscillation prediction for the reactor data sets, especially at low energy, substantially improve the fits and reduce the tension. We consider two such scenarios. The first introduces one sterile neutrino (3+1) and the Quantum Mechanical wavepacket effect that accounts for the source size in reactor experiments. We find that inclusion of the wavepacket effect greatly improves the overall fit compared to the null model by $\Delta\chi^2/\text{dof} = 60.2/4$ (7σ improvement) with best-fit $\Delta m^2 = 1.4 \text{ eV}^2$ and wavepacket length of 67 fm; internal tension is reduced to 3.6σ . If reactor-data only is fit, that the wavepacket preferred length is 91 fm ($> 20 \text{ fm}$ at 99% CL). The second model introduces oscillations involving sterile flavor and allows the decay of the heavier, mostly sterile, mass state ν_4 . This model introduces a damping term similar to the wavepacket effect, but across all experiments. Compared to null, this has a $\Delta\chi^2/\text{dof} = 60.6/4$ (7σ improvement) with preferred $\Delta m^2 = 1.4 \text{ eV}^2$ and decay $\Gamma = 0.35 \text{ eV}$; and internal tension of 3.7σ .

For many years, the reactor event rates have been observed to have structure that deviates from prediction. Community discussion has focused on an excess compared to prediction observed at 5 MeV; however, other deviations are apparent. This structure has L dependence that is well-fit by the damped models. Before assuming this points to new physics, we urge closer examination of systematic effects that could lead to this L dependence.

I. INTRODUCTION

Since 1995, a series of experiments searching for neutrino oscillations have reported potential oscillation signals with 2σ to 5σ significance with squared-mass splittings, Δm^2 , of $\mathcal{O}(1 \text{ to } 10 \text{ eV}^2)$. These results do not fit our present picture of neutrino oscillations, which involves only three neutrinos; hence, with only two mass splittings that are presently measured to be $7.4 \times 10^{-5} \text{ eV}^2$ and $2.5 \times 10^{-3} \text{ eV}^2$ [1], based on oscillation signatures well-exceeding 5σ . Thus, taking the results at face value, these results represent anomalies that may be pointing to new physics. The simplest new physics solution introduces one additional neutrino that does not interact with the W and Z bosons, and hence is called “sterile” [2] but does participate in oscillations. This model is called 3+1.

For the last decade, the 3+1 model has been challenged in multiple ways. First, a set of experiments following up on the anomalies have excluded signals due to the 3+1 scenario. Some experimental data sets suffer internal inconsistencies with a neutrino-scattering description. Also, global fits to the full data set have shown this suffers internal inconsistencies, commonly called “tension.” [3–5] As a result, most of the community has reached the view that the simple 3+1 model cannot explain the data [6].

This article presents global fits that look beyond simple 3+1 models. In particular, we explore expanding beyond the plane-wave description of simple 3+1 to include “wavepacket effects” that take into account the finite size of the source producing the neutrino, which was first discussed in this context in Ref. [7]. These effects show up as decoherence in experiments that have a relatively long L/E . In the case of the experiments in the global fits, this will most affect reactors, damping the oscillation prediction at low energy. Here, we show that this model, called “3+1+WP” to distinguish from the plane-wave 3+1 model, considerably reduces the tension in global fits. We show that this solution, which does not involve introducing additional new Beyond Standard Model (BSM) physics to 3+1—it simply draws on known expectations from Quantum Mechanics—improves the fits more than models that introduce additional sterile neutrinos, 3+2 or 3+3.

We also revisit a more complex model that has been examined in the past that introduces decay of the highest mass state in a 3+1 model, ν_4 [5, 8, 9]. The concept behind “3+1+dk” models is that while the sterile neutrino does not carry Standard Model couplings, it may carry Beyond Standard Model couplings to other new particles and/or to Standard Model particles. In this case, one can expect decay, which will most affect the highest mass state due both to the larger mass and to the large sterile content from the mixing matrix. Decay of the ν_4 state damps oscillations at the largest mass splitting, and

* jmhardin@mit.edu

this affects all data sets, not just the reactor data sets. However, we show that the best fit 3+1+dk parameters damp the reactor results while not substantially changing the prediction for other data sets leading to a very similar result as 3+1+WP.

The work presented here builds on 15 years of global analyses [10–13], and especially our analysis from 2019 [5]. The 2019 paper provides a pedantic review of the theory and practice of sterile neutrino fits; therefore, in Sec. II, we describe the limitations of and extensions to the simple 3+1 model only briefly. In Sec. III, we focus on the latest information that has been included in the results, which involves several new data sets and some substantial updates. In Sec. IV, we only briefly discuss the methods of fitting and expressing the quality of fits, and the reader should see Ref. [5] for details.

Although the reactor experiment data have only been modestly updated since 2019, in Sec. III we extend a discussion begun in Ref. [5] concerning whether features in the reactor spectrum can obscure fit results; see Ref. [14] for a similar recent discussion in the context of accelerator neutrinos. Attention has focused on one feature of the reactor event energy spectrum, which is an excess at 5 MeV; however, the entire spectrum suffers many more excesses and deficits that vary from experiment to experiment. The reactor community has taken ratios in various ways to reduce systematic pulls in sterile neutrino fits from these effects, in spite of that we will show that suspicious structure that may not be related to Beyond Standard Model effects remain and are not identical between data sets and are not well covered by the systematic uncertainty provided in data releases for global fits. We flag this because this may explain why damped models like 3+1+WP and 3+1+dk may be preferred.

In Sec. V, we present the latest global-fit results. These will show a preference for damped models for reactors. We show that these models substantially improve the well-known tension between the appearance data subset and disappearance data subset. Though some tension remains and we will show the bulk of this tension can be attributed to the MiniBooNE data set. As we note in Sec. III, the MiniBooNE data is well-known for appearing to have two contributions to the excess, one of which matches the kinematic expectations for ν_e scattering, as expected from oscillations, and one of which is forward peaked, so the tension from MiniBooNE was expected.

Finally, in Sec. VI, we revisit the information summarized above with more detail, in light of the quantitative results of Sec. V.

II. STERILE NEUTRINO MODELS

The neutrino-extended Standard Model has three active neutrino flavors engaging in oscillations. This is referred to as the “null” model in this study. We will compare the models discussed below involving sterile neutrinos to the null model. In this section, we introduce the

examples used in our fits. We also discuss metrics for comparing models.

A. Frequently Used Sterile Neutrino Models: Plane-wave “3+1” and “3+N”

The community standard for comparing sterile neutrino searches has used 3+1 models. In this model, the Pontecorvo-Maki-Nakagawa-Sakata (PMNS) mixing matrix is expanded by one row and one column to accommodate the new flavor state (“s”) and mass state (“4”):

$$U_{3+1} = \begin{bmatrix} U_{e1} & U_{e2} & U_{e3} & U_{e4} \\ \vdots & & \vdots & U_{\mu 4} \\ \vdots & & \vdots & U_{\tau 4} \\ U_{s1} & U_{s2} & U_{s3} & U_{s4} \end{bmatrix}. \quad (1)$$

The short-baseline approximation is also frequently used, where $\Delta_{41}^2 \gg |\Delta_{31}^2| > \Delta_{21}^2$ is assumed and that the measured L/E is small enough that only the oscillation due to Δ_{41}^2 is observable. The result is that the oscillation probabilities for ν_e disappearance, ν_μ disappearance, and ν_e appearance are connected:

$$P_{\nu_e \rightarrow \nu_e} = 1 - 4(1 - |U_{e4}|^2)|U_{e4}|^2 \sin^2(\Delta_{41}L/E), \quad (2)$$

$$P_{\nu_\mu \rightarrow \nu_\mu} = 1 - 4(1 - |U_{\mu 4}|^2)|U_{\mu 4}|^2 \sin^2(\Delta_{41}L/E), \quad (3)$$

$$P_{\nu_\mu \rightarrow \nu_e} = 4|U_{e4}|^2|U_{\mu 4}|^2 \sin^2(\Delta_{41}L/E), \quad (4)$$

where $\Delta_{41} = 1.27\Delta m_{41}^2$. In this case, L and E are in units of m and MeV (or km and GeV), respectively. A consistent 3+1 global fit requires signals in all three of these oscillation modes with the same large mass-square splitting, Δm_{41}^2 . One also sees that the probabilities of appearance and disappearance must be related through a consistent set of matrix elements.

The above equations are often re-written by replacing the combinations of matrix elements with “pseudo-mixing-angles:

$$P_{\nu_e \rightarrow \nu_e} = 1 - \sin^2 2\theta_{ee} \sin^2(\Delta_{41}L/E), \quad (5)$$

$$P_{\nu_\mu \rightarrow \nu_\mu} = 1 - \sin^2 2\theta_{\mu\mu} \sin^2(\Delta_{41}L/E), \quad (6)$$

$$P_{\nu_\mu \rightarrow \nu_e} = \sin^2 2\theta_{\mu e} \sin^2(\Delta_{41}L/E). \quad (7)$$

In this article, we will present the results of the global fits within the context of these pseudo-mixing-angles.

Although 3+1 is the standard that is used for searching for new physics in short-baseline experiments, it is chosen for its ease of application to fits rather than because there is strong motivation to have only one sterile neutrino. A less minimal model expands the sterile neutrino model to include a second sterile neutrino in the model (“3+2”). Immediately, 4 new parameters are added to the theory. Fits to the most “natural” case, with three sterile neutrinos (“3+3”) become even more complicated, with a further 5 parameters added to the theory. The equations for 3+2 are provided in Ref. [5], which also presents 2019 results showing that 3+2 does not substantially improve matters.

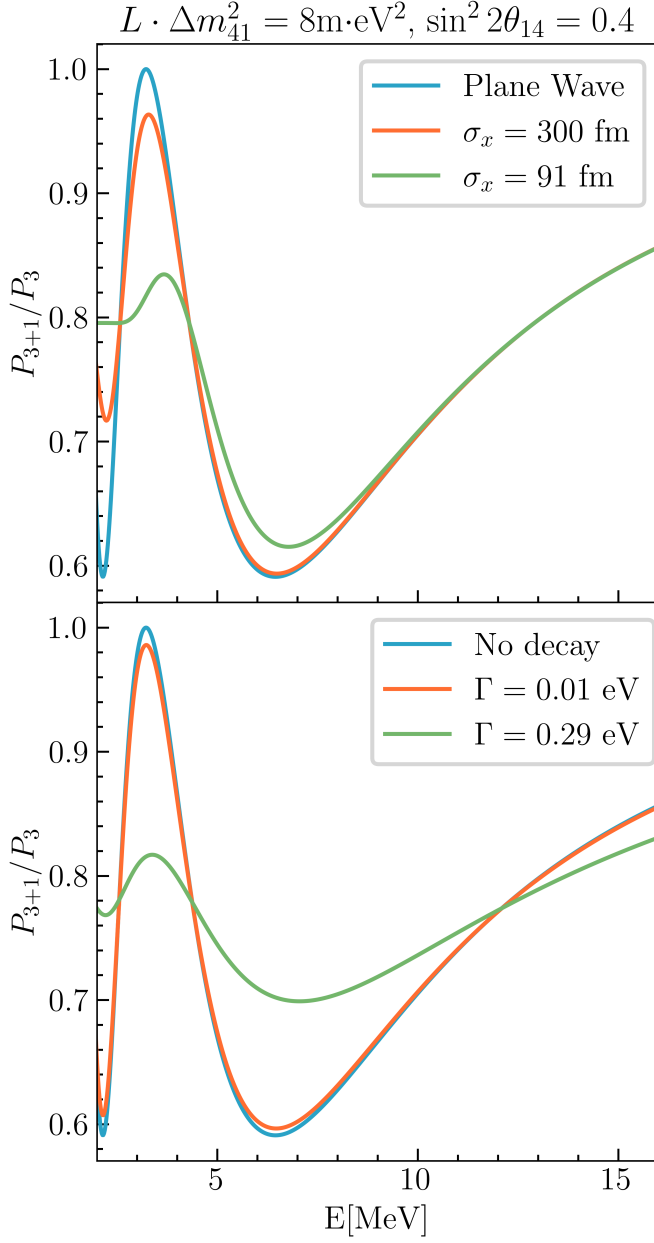


FIG. 1. Illustration of the damping of oscillations from the wavepacket effect (top) and from decay (bottom). The ratio of 3+1 to three neutrino oscillation probabilities is shown as a function of energy for fixed $L\Delta m^2$, which for a reactor experiment at $L = 8 \text{ m}$ corresponds to $\Delta m^2 = 1 \text{ eV}^2$ —a case relevant to this study. 3+1, which is a plane-wave model, is shown in blue. The orange and green curves are examples of modest and extreme damping at low energy for the 3+1+WP and 3+1+dk models.

B. Including Wavepacket Effects (“3+1+WP”)

The 3+N models describe neutrinos as plane waves, where the interference between the massive states happens at any point in the space along the neutrino trajec-

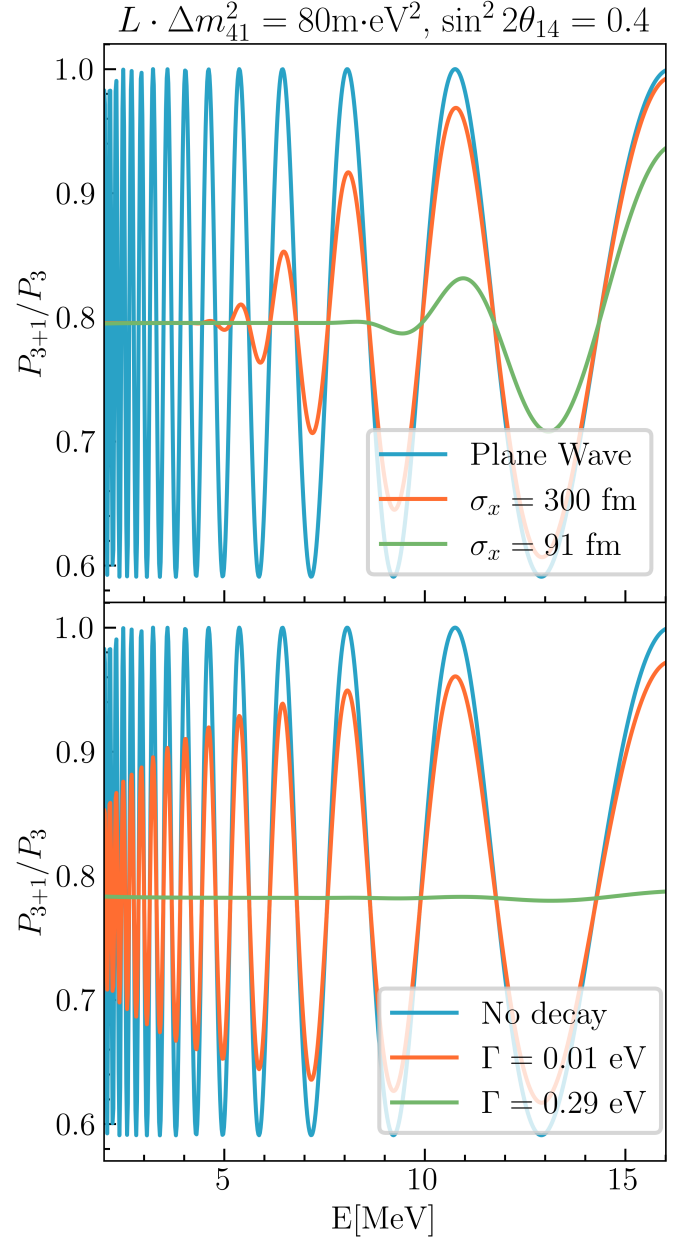


FIG. 2. Illustration of the damping of oscillations from the wavepacket effect (top) and from decay (bottom), as with Fig. 1, but for $\Delta m^2 = 10 \text{ eV}^2$. In this case, damping occurs across all energies.

tory. That description of the neutrino evolution is simplistic because it does not take into account that neutrinos are localized particles produced by a source of finite size. This introduces a “wavepacket effect”: as the neutrino propagates, the difference in the group’s velocity of each massive state will result in a separation between them. After some distance, the mixing between the massive state will stop, the oscillation will cease and the evolution can be described as an incoherent superposition of massive states. The distance where the decoherence

starts having an effect on the oscillation is given by the decoherence length given by

$$L^{\text{coh}} = 0.566\text{m} \left(\frac{E}{\text{MeV}} \right)^2 \left(\frac{\sigma_x}{100\text{fm}} \right) \left(\frac{\text{eV}^2}{\Delta m^2} \right), \quad (8)$$

that depends on the neutrino energy (E in MeV), the characteristic size of the wave packet (σ_x in 100 fm), and the squared neutrino mass difference (Δm^2 in eV^2). The effect manifests as a characteristic “damping effect” at low values of the energy distribution if $L\Delta m^2$ is much larger than E .

The wavepacket effect is a Standard Model Effect that will show up within any oscillation data set at some level, though it may be too small to be observed if the size of the source producing the neutrinos is very small. Among today’s three-neutrino oscillation experiments, the set that is expected to be most affected is reactor experiments, where the characteristic length of the U and Pu nuclei ($\mathcal{O}(10\text{ fm})$) and the interatomic spacing (10^5 fm) each may contribute. A fit to Daya Bay, RENO, and KamLAND data, set a limit on the wave-packet width of $\sigma_x > 210\text{ fm}$ at 90% CL [15]. This constraint is largely driven by KamLAND due to its large L/E ; if only RENO and Daya Bay are used in the fits then the limit is $\sigma_x > 100\text{ fm}$ at 90% CL [16]. As recently noted in Ref. [17] this constraint will be improved by the upcoming JUNO experiment.

In a 3+1 model, this effect is included following the method of Ref. [7], with the electron-flavor disappearance probability modified to be [7]:

$$P_{\nu_e \rightarrow \nu_e}^{\text{WPP}} = 1 - \sin^2 2\theta_{ee} \left[\left(\frac{1 - e^{-A^2}}{2} \right) + \sin^2(\Delta_{41} L/E) e^{-A^2} \right], \quad (9)$$

where $A = L/L_{\text{coh}}$ and L_{coh} proportional to σ_x as seen in eq. 8. If σ_x is sufficiently small enough, the effect becomes observable.

Figs. 1 and 2, top, illustrate the effect of varying σ_x on the predicted signal for a reactor experiment located at $L = 8\text{ m}$, for $\Delta m^2 = 1$ and 10 eV^2 , respectively. The predictions for the models are shown as a ratio to the null model. The blue line is a 3+1 (plane wave) model. The orange line shows a moderate example for σ_x and the green shows a value close to the limit from Ref. [15]. Fig. 1 shows that at small Δm^2 , the damping occurs at low energy, while Fig. 2 shows that at large Δm^2 , the damping will occur across the entire relevant energy range for reactors.

We note that there is some ongoing controversy on the theoretical prediction for the size of the wavepacket effect [18–21]. We encourage the theory community to continue this discussion as its resolution is key in understanding the role of reactors in light sterile neutrino searches [7] and the determination of the neutrino mass ordering [17]. We do not choose to consider any theoretical prediction, and instead investigate this question

in an agnostic, experiment-driven manner as in Ref. [7]. Specifically, we will perform global fits to the 3+1+WP, applying the wavepacket scenario only to reactors, allowing σ_x to float. We will then compare that result to those fits from Refs. [15, 16]. As discussed below, our findings are that a small value of σ_x , which causes strong damping for the reactor results (Green case in Fig. 2), is preferred. Finally, we also encourage the reader to see Ref. [22] and references therein for beyond Standard Model mechanisms that effectively change the neutrino wave packet size.

C. 3+1 with decay (“3+1+dk”)

The wavepacket effect is not the only way to introduce damping into the 3+1 picture. A second model which causes damping is allowing neutrino decay and is called “3+1+dk”. Unlike the wavepacket effect, which is a quantum-mechanical effect one expects in oscillations, this model explicitly expands the new physics of the 3+1 model. Also, unlike the wavepacket effect, this will potentially introduce damping across all experiments, regardless of the source of the flux.

The phenomenological motivation for 3+1+dk is that the existence of neutrino mass also permits decay of the mass state if the “sterile” neutrino has Beyond Standard Model interactions. The possibility of decay of ν_4 , the primarily-sterile state, has been considered in many references [9, 23–35]. Sterile neutrino decay leads to a damping in the neutrino oscillation patterns in L/E , as well as production of new beyond-Standard Model particles and of known particles such as photons, or of ν_1 , ν_2 and ν_3 , thereby regenerating the flux. In this article, we will only consider the damping effect on oscillation signals.

The experimental motivation for 3+1+dk came from analysis of IceCube ν_μ disappearance data [36]. The IceCube collaboration found that their atmospheric ν_μ data were fit better with 3+1+dk than 3+1, and that 3+1 was a slightly better fit than null. Thus, an important point of departure from the 3+1+WP model is that 3+1+dk is applied to all data sets, not just the reactor data set. The survival probability for the ν_e disappearance case is given by:

$$P_{\nu_e \rightarrow \nu_e}^{3+1+dk} = 2|U_{e4}|^2 e^{-2.53 \frac{m_4 L}{\tau E}} (1 - |U_{e4}|^2) \cos(2.53 \Delta m_{41}^2 (L/E)) + |U_{e4}|^4 e^{-5.07 \frac{m_4 L}{\tau E}} + (1 - |U_{e4}|^2)^2, \quad (10)$$

where $m_4 = \sqrt{\Delta m_{41}^2}$, since the smallest mass state is assumed to have negligible mass. The other oscillation probabilities are modified in a similar manner. The decay causes the ν_4 state to die away as a function of L/E , so experiments with relatively large L/E , like the reactor experiments, become insensitive to oscillations.

We illustrate the 3+1+dk effect on reactors in Figs. 1 and 2, bottom. As described for the wavepacket illustration, the orange and green represent modest ($\Gamma =$

	$\nu_\mu \rightarrow \nu_e$	$\nu_\mu \rightarrow \nu_\mu$	$\nu_e \rightarrow \nu_e$
ν	MiniBooNE NUMI-MB NOMAD MicroBooNE	SciBooNE-MB CCFR CDHS MINOS MicroBooNE	KARMEN-LSND-xsec SAGE+GALLEX BEST MicroBooNE MiniBooNE
$\bar{\nu}$	LSND KARMEN MiniBooNE	SciBooNE-MB CCFR MINOS IceCube	Bugey NEOS DANSS PROSPECT STEREO MiniBooNE

TABLE I. The data sets used in global fits presented in this article, divided according to the type of fit applied. Citations for data sets are provided in the text.

0.01 eV) and extreme ($\Gamma = 0.29$ eV) values of the damping parameter. One sees that moderate values of Γ will damp at large Δm^2 and not small Δm^2 , while larger values damp across the full energy range.

III. INPUTS TO THE GLOBAL FITS

Table I maps all data sets used in this analysis to the type of fit that applies. Compared to the fits presented in Ref. [5], the fits in this article include new experiments and updates to previous experiments. The experiments added were: BEST [37], STEREO [38], and MicroBooNE [39]. The MiniBooNE [40], MINOS+ [41], and IceCube [42] results have been substantially updated. The remaining citations for experiments that are not updated, and are described in detail in Ref. [5], are Refs. [43–54].¹

In this section, we comment on issues in both the new and updated data sets. We note that anomalies are appropriately given very careful scrutiny, and discuss some examples. However, limits tend to receive less scrutiny by the community—a bias that can potentially lead to misconstruing the information from the data. In this article, we look more carefully at limits from MINOS+ and from the reactor experiments. The discussion of reactor results is especially pertinent to the conclusions of this work.

A. New to These Fits: MicroBooNE

The MicroBooNE experiment released first results probing the electron neutrino interpretation of the Mini-

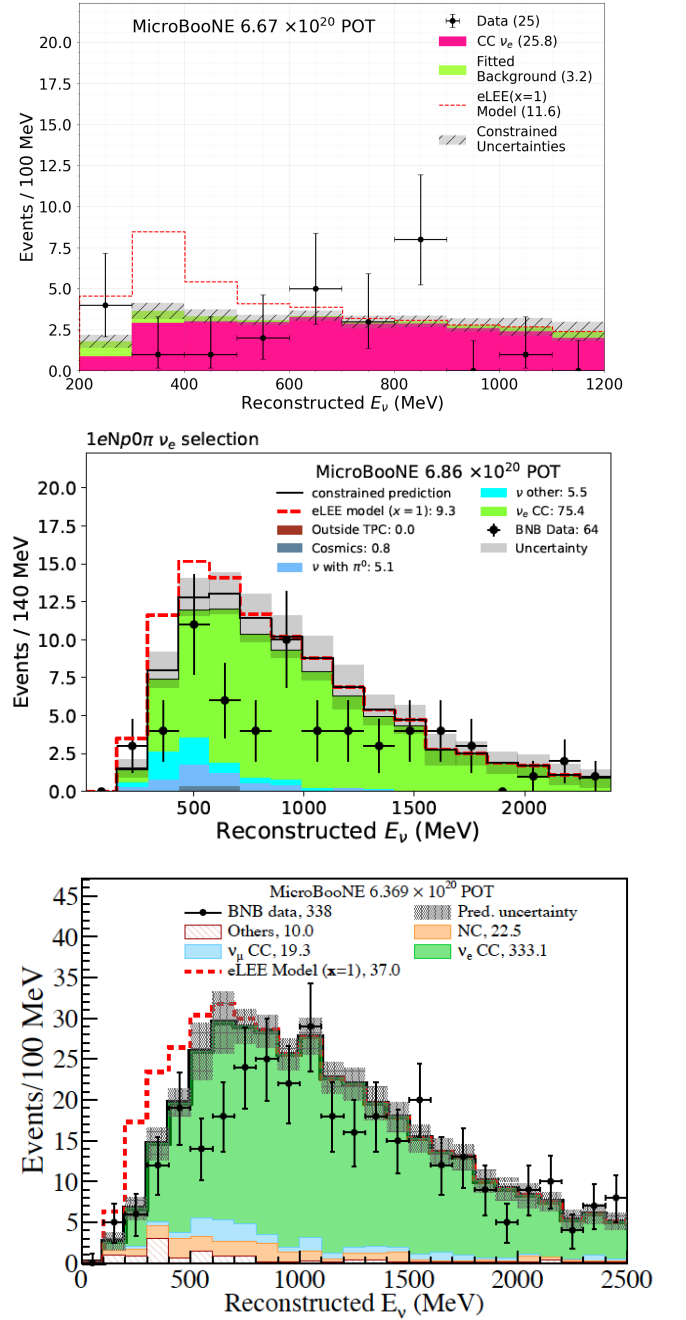


FIG. 3. MicroBooNE ν_e energy spectra from Ref. [39] from the CCQE analysis, top; semi-inclusive analysis, middle; and inclusive analysis, bottom.

BooNE excess in October 2021 [39]. Three analyses looked for an excess of electron neutrinos in the Booster Neutrino Beam, focusing on (1) an exclusive sample of ν_e CCQE-like events with one electron and one proton in the final state, (2) a semi-inclusive sample of MiniBooNE-like ν_e CC events with no pions in the final state, and (3) an inclusive sample of all ν_e CC interactions. The results were very surprising, indicating a deficit of ν_e with respect to the Standard Model [57], not an excess. Due to

¹ We have not included data from Neutrino-4 [55] because we were not able to reproduce their results based on the information that they have provided, and the authors did not respond to our questions. The problems with treatment of Neutrino-4 data that we identified agrees with those observed in other studies [56].

this surprise, we discuss how we handle this data set in some detail.

The ν_e energy distribution for the three samples is shown in Fig. 3 [39]. One can see that there is a substantial deficit that is $\sim 2\sigma$. The source of this deficit is unclear, but it can be interpreted as a signature for 3+1 oscillations with ν_e disappearance. The ν_μ data, on the other hand, is higher than prediction [39].

Fits to 3+1 by scientists outside of the MicroBooNE following publication of this result [40, 57, 58], led MicroBooNE to release internal fits to this data within the 3+1 model in October 2022 [59]. All of these results lead to the same conclusion: because MicroBooNE has a deficit for ν_e , the 3+1 limits from the data are not very strong and, when combined with MiniBooNE, do not significantly change the result from a fit to MiniBooNE alone [40, 58]. In this study, we use the released data from Ref. [39], because Ref. [59] is not yet published and the data is not yet released. However, we note that Ref. [59] sets even weaker limits on 3+1 than our result, which matches Ref. [40, 58], so our approach is slightly conservative.

To be specific on our approach, we have calculated constraints on the 3 + 1 model from both the exclusive CCQE-like and the inclusive analyses, as the MiniBooNE-like analysis has not provided a public data release. This is a reasonable representation of MicroBooNE's first results, as the two included analyses are the most sensitive to eV-scale sterile neutrinos. These two analyses are not statistically independent, and it is not straightforward to estimate correlations between the two analyses. Therefore, we consider only the inclusive analysis in the global fit, as it provides the strongest constraints on the 3 + 1 model.

In order to estimate the MicroBooNE prediction under a given 3 + 1 hypothesis, we follow the procedure outlined in Ref. [40]. Specifically, we leverage information from the MiniBooNE Booster Neutrino Beam simulation to derive the prediction in four of the seven samples of the MicroBooNE inclusive analysis: ν_e and ν_μ fully-contained and partially-contained events. This is limited by the data release, which does not include information of the remaining three π^0 -based samples [60].

For the statistical treatment of the inclusive analysis, we use the combined Neyman-Pearson χ^2_{CNP} [61]. This test statistics attempts to incorporate finite Monte Carlo statistics in the small sample size regime, we encourage the reader to review Refs. [62–66] for further discussion of this topic. We use the joint covariance matrix provided by MicroBooNE to account for correlations between the four different samples [60].

We also consider two additional nuisance parameters to account for potential additional uncertainty in the relative efficiency of the ν_e and ν_μ channels of the inclusive analysis. This is motivated by systematic disagreement between data and prediction in the ν_μ channels. The introduced nuisance parameters adjust the overall normalization of the prediction in the ν_μ FC and PC chan-

nels. We consider a flat prior bounded within $\pm 1\sigma$ of the nominal prediction in the channel, where σ is defined as the uncertainty on the overall normalization in each channel calculated from the reported covariance matrices. The nuisance parameters are unpenalized within the $\pm 1\sigma$ window and thus effectively re-scale the overall normalization in each ν_μ channel under a given 3 + 1 model hypothesis toward the observed data (bounded by $\pm 1\sigma$ of the nominal normalization). This is important for the ν_μ disappearance result, as the inclusive analysis sets much stronger constraints on $\sin^2 2\theta_{\mu e}$ compared to their sensitivity when these nuisance parameters are not included. Introducing the parameters relaxes the observed constraint to more closely match the sensitivity. One could in principle achieve the same effect through a proper Feldman-Cousins interpretation of the inclusive analysis statistical results; however, this is prohibitively difficult in the context of the current global fit.

With this said, we flag a concern about the MicroBooNE ν_e data set. Along with the oscillation studies, MicroBooNE has also published ν_e cross section results that show that a substantial portion of the deficit appears in highly-forward-going proton events [67]. The deficit of these forward-proton events is not explainable by cross section models and may be inconsistent with simple two-body scattering kinematics. However, it is also unlikely to be due to an oscillation effect. Rather than new physics, this forward-proton deficit may be pointing to an unmodelled inefficiency in the detector. That might not be surprising, since liquid argon TPC (LArTPC) detectors are state of the art and this is the first analysis attempting to understand electromagnetic showers and forward-going protons at these energies. At present, the question of whether MicroBooNE has an unmodelled detector inefficiency is not an urgent issue because the data set has small statistics and is relatively weak in the fits. But careful scrutiny will be called for in the future as more LArTPC experiments turn on, adding to the statistics from LArTPC detectors. We also note that if this is a detector effect, this may also represent a problem for DUNE ν_e appearance physics.

B. New to These Fits: BEST

The Baksan Experiment on Sterile Transitions (BEST) experiment ran to follow up on the Gallium anomalies [68]. In 2019, a (3.414 ± 0.008) MCi ^{51}Cr source was placed in the center of a dual volume gallium detector. The inner spherical volume of diameter 133.5 cm held 7.5 tons of Ga, while the outer cylindrical volume with dimension $(h, \rho) = (234.5, 109)$ cm held 40.0 tons.

Like the previous Gallium anomalies, BEST observed a deficit Ge production rate in both volumes, with ratios of $R_{\text{in}} = 0.791 \pm 0.05$ and $R_{\text{out}} = 0.766 \pm 0.05$. The deficits are between 4σ and 5σ , which is very large compared to results from most electron-flavor experiments. This new addition to our fits joins two other data sets with $> 4\sigma$

signals, LSND and MiniBooNE.

The data-to-predicted ratio between the two volumes is 0.97 ± 0.07 , which is consistent with unity. Therefore, an overall deficit is observed, but there is no clear oscillatory effect between volumes. However, oscillations may be rapid compared to the L in each volume, which would average out the signal for relatively high Δm^2 . Averaging due to rapid oscillations produces damping for large L/E .

In combination with the previous Gallium anomalies, a strong preference for ν_e oscillation is found with a large mixing angle of $\sin^2 2\theta = 0.34$ recovered for $\Delta m^2 \gtrsim 1 \text{ eV}^2$. This result does not include wavepacket effects, and we will not include wavepacket effects in our global fits, though we note that Chromium is a moderately large nucleus. Ref. [7] explores wavepacket effects in this data set and an observable effect is found to be very modest for two reasons. First, it is a counting experiment, and second, the relative size of the two volumes leads to L -averaging across most of the region of interest in Δm^2 , dominating damping effects from 3+1+WP.

C. Updated for These Fits: IceCube

The sterile neutrino analysis with the IceCube Neutrino Observatory near the geographical South Pole studies neutrinos events that span an energy range from approximately 500 GeV to 10 TeV and examines the northern hemisphere. The IceCube analysis examines observed ν_μ event rate for upward, through-going interactions below the detector and contained interactions within the detector. The data are analyzed as a function of reconstructed neutrino energy, which has a large smearing for events below the detector, and zenith angle, θ_z . The zenith angle plays the role of L in the usual oscillation analysis.

A deficit in this data set would arise from matter-induced effects as well as vacuum oscillations, hence this data set is very different from the rest listed in Table I, which are all subject to only vacuum oscillations. At TeV energies, in the presence of a light sterile neutrino, matter-enhanced resonances producing deficits of events are expected to appear in the energy vs. $\cos \theta_z$ event plane. The location of the resonance disappearance depends on the mass-square difference, Δm_{41}^2 and mixing angle, θ_{24} . For small mixing angles the resonance happens for core-thoroughgoing trajectories, while for larger mixing they can extend to the mantle region. The mass splitting controls the resonance location in energy, where the larger the difference the higher the resonance energy. See Ref. [69] for an extended discussion.

To date, the global fits where we have included IceCube results encompassed only 1 year of data [13, 70]. However, recently IceCube has supplied data releases for eight years of data analyzed in a 3+1 scenario [71] and in a 3+1+dk scenario [72]. These latest analyses used an improved event selection and systematic treatment described in Ref. [73]. Notable improvements in systematic

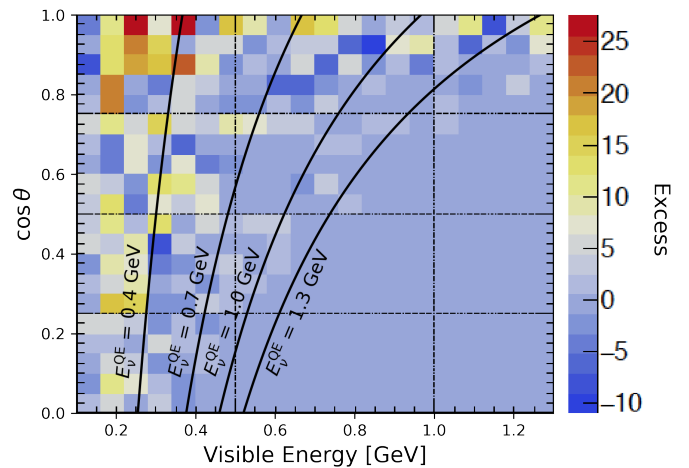


FIG. 4. The MiniBooNE excess is described as a function of E_{vis} and $\cos(\theta)$, where θ is the electron scattering angle, from Ref. [76]. We have annotated the plot by adding lines of constant E_ν . If the sample were strictly due to ν_e charged current quasielastic scattering, the events would be distributed along these curves according to the neutrino energy prediction. While true of about half the event sample, one notes a cluster of events at $\cos(\theta) > 0.9$ and low energy that deviates from expectation. The origin of this cluster is not yet identified.

treatments include an improved treatment of the atmospheric flux uncertainties [74] and a new treatment of the bulk ice uncertainties [75]. To date, IceCube has only released likelihoods with these specific models and not bin-by-bin event rates compared to Standard Model. As a result, this data release can only be interpreted within in 3+1, 3+1 with wavepacket (since for IceCube this will be degenerate with 3+1), and 3+1+dk. The likelihoods are not available for 3+2 and 3+3 fits and are not included in our analysis.

D. Updated for These Fits: MiniBooNE

For these global fits, we use the final MiniBooNE data set that was released in 2022 [76]. We have updated our analysis to account for all 3+1-related phenomena, $\nu_e/\bar{\nu}_e$ appearance and disappearance as well as $\nu_\mu/\bar{\nu}_\mu$ disappearance, matching the treatment outlined in Ref. [40]. In Ref. [76], the MiniBooNE collaboration noted that the ν_e excess in the data appears to have two contributions, one that follows the expectation of CCQE scattering and one that is at low energy and more forward peaked than expected. The two contributions are indicated in Fig. 4.

This observation has led to exploration of a potential “Altarelli Cocktail” where a collection of systematic effects all combine to produce an effect [77, 78]. The latest of these results argue that only 3σ of the 4.8σ excess may be oscillations with the rest due to a small unaccounted contribution from 2p2h process (in the authors’ Mini-

BooNE analysis it reduces the significance from 4.69σ to 4.27σ) and systematic effects associated to the inferred $\text{NC}\pi_0$ event rate. The authors of Ref. [78] mimic $\text{NC}\pi_0$ misidentification probability by means of constructing cuts on the visible energy and direction of the produced photons, which is an approximation of the full likelihood-based analysis used by the collaboration. Their method is found to be in good agreement with the collaboration provided distributions. They argue that the cut placed on this likelihood was too weak due to an underfluctuation of the Monte Carlo distribution used in deriving it. However, as noted by the authors, this argument relies on behavior on specific parts of kinematic phase space as well as the behavior of the efficiency at the tails. They find that depending on which generator is used this can change the significance from 4.7σ to 3.6σ when the same event generator is used; the use of other event generators with the authors' cuts does not further reduce the significance. The authors find a large variability of the significance when trying different sets of cuts and generators, this highlights the point that the tails of the distributions are relevant here implying that only a full collaboration reanalysis using their specific likelihood function can yield proper assessment of the impact of finite sample size Monte Carlo. The behavior of small sample size in Monte Carlo statistics has been discussed in Ref. [64–66] and implies that the distributions are non-Gaussian in nature. This is a problem since short-baseline accelerator experiments, such as MicroBooNE, use covariance matrices to describe the experimental uncertainties. This prescription, by construction, assumes that the systematic uncertainties have Gaussian behaviors which is not the case for finite Monte Carlo uncertainties. Note that this does not affect experiments such as IceCube, which uses methods given in [65] and implements systematic uncertainties via nuisance parameters. Alternatively, the excess of photons in the low-energy could potentially be explained by a mixed model involving oscillations and new physics, where representative examples are Refs. [79, 80] or other similar models where additional photons are produced.

Both approaches are in agreement with the MicroBooNE limit on the MiniBooNE excess as consisting of $< 51\%$ ν_e interactions [39], though that limit is affected by the deficit of ν_e observed in MicroBooNE as discussed above. For the fits here, we will assume an explanation for MiniBooNE that is fully due to oscillations. However, we will show that MiniBooNE does contribute at a substantial level to the tension measured in the results, as discussed in Sec. IIB, and this would be consistent with a mixed-model explanation.

E. Updated for These Fits: MINOS+

Long-baseline (LBL) experiments take advantage of measuring the neutrino flux from a well-defined direction and baseline to determine the oscillation parameters with good precision. To reduce the uncertainties related

to the flux and cross-section, LBL experiments typically use a near/far configuration, where the flux is measured at two different baselines. In the case of MINOS+ [41], the neutrino flux generated in the NuMI beam is measured in a near detector at a 1.04 km baseline and in a far detector at 735 km.

The flux peaks at ~ 3 GeV, but extends over a wide energy range from 0.5 GeV to 40 GeV, which allows constraints on Δm_{31}^2 and $\sin^2 \theta_{23}$ [81] within the 3ν -mixing scenario. In the $3+1$ scenario, the broad energy range makes it possible to study a large range of masses. The oscillation length is comparable to the distance to the far detector for $\Delta m_{41}^2 \in [10^{-3}, 10^{-1}] \text{eV}^2$. The oscillation will happen at shorter distances for larger masses. For $\Delta m_{41}^2 \in [1, 50] \text{eV}^2$, the neutrino will show a flavor oscillation in the near detector. In the far detector, the new phase will be too large to be resolved by the detector resolution, and it will average out. For masses above $\sim 50 \text{eV}^2$, the oscillation length is shorter than the distance to the near detector, and the oscillations will also be averaged out in the near detector. being the oscillation introduced by the sterile neutrino

The combined analysis between MINOS and MINOS+ [82], which correspond to an exposure of 16.36×10^{20} POTs, excludes $\sin^2 \theta_{24} > 5 \times 10^{-3}$ for masses between $10^{-2} \text{eV}^2 < \Delta m_{41}^2 < 10 \text{eV}^2$ at 90% CL (See Fig 5). Above $\Delta m^2 > 10 \text{eV}^2$ mixings larger than $\sin^2 \theta_{24} > 2 \times 10^{-2}$ are excluded. The value of the “Official” $\sin^2 \theta_{24}$ limit for $\Delta m^2 > 100 \text{eV}^2$ corresponds to a flux normalization uncertainty of $\sim 4\%$ due to the average over the fast oscillations. This is almost a factor 2 times smaller than the $\sim 8\%$ normalization included in MINOS+ analysis [82] and suggests that, in the large mass regime, the sensitivity to $\sin^2 \theta_{24}$ comes from a feature in the event distribution instead of from the normalization uncertainty.

The wide range of energies covered by the event rate in MINOS+ encodes different types of neutrino interaction covering the quasi-elastic regime at energies below ~ 2 GeV, the resonant production of mesons at ~ 4 GeV, and the scattering with the quarks in the DIS regime at energies above ~ 10 GeV. The agreement between the MC prediction and the data for the charge currents events is shown in Fig. 6 for $\Delta m_{41}^2 = 10^3 \text{eV}^2$ and $\sin^2 \theta_{24} = 0.025$ for the near and far detectors. We can consider the MINOS data set in the two interaction-type regimes, < 12 GeV and > 12 GeV. At < 12 GeV, there appears to be an offset in energy between the near and far detector, as one can see in the ratio plot. We correct this in the fits by including a free parameter for an energy miscalibration and find a 10% effect. For > 12 GeV both the prediction and data are relatively flat but have a large normalization difference that is not seen at low energy. As a result, we fit the two regimes for oscillations, above and below 12 GeV, separately. The results of the analysis are shown in Fig. 5.

The high energy sample (orange line) dominates the sensitivity to $\sin^2 \theta_{24}$ for masses between $10^{-2} \text{eV}^2 <$

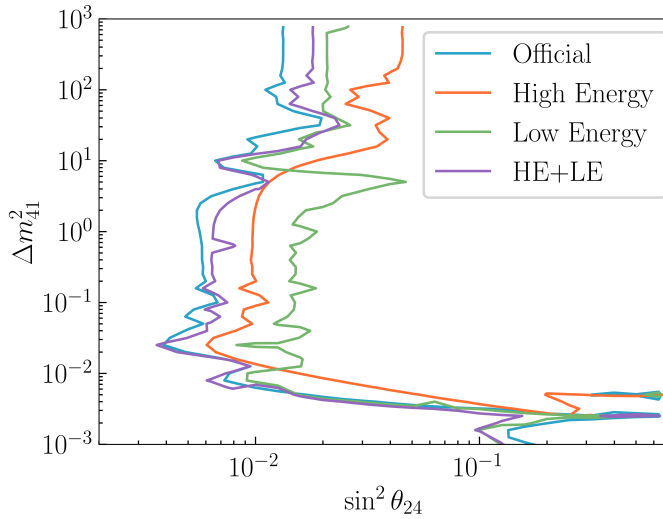


FIG. 5. Analysis of MINOS and MINOS+ data [82]. We show the official result from the collaboration (blue), and the analysis of the low-energy (green) and (high) energy samples (red). For the low-energy sample analysis, a systematic that accounts for miss-reconstructed energy in the near detector is included. The combined analysis between the low-energy and high-energy samples is shown in line purple.

$\Delta m_{41}^2 < 10 \text{ eV}^2$, excluding mixings larger than $\sin^2 \theta_{24} > 10^{-2}$. Above 10 eV^2 , the excluded value rises to $\sin^2 \theta_{24} = 0.045$, corresponding to a deviation in the flux normalization of 8.5%. The minimum χ^2 in the high-energy sample is $\chi_{min,HE}^2 = 31.9$.

The sensitivity in the high-mass region is dominated by the low-energy sample (green line), which excludes $\sin^2 \theta_{24} > 0.02$, when we include the energy miscalibration of $\sim 10\%$, discussed above. The minimum χ^2 of the low energy sample is $\chi_{min,LE}^2 = 41.6$, rising to $\chi_{min,LE}^2 = 51.3$ if the systematic uncertainty related to the reconstructed energy in the near detector is not included.

The combined analysis of the high-energy and the low-energy samples is given by the purple line, and the minimum $\chi_{min,LE+HE}^2 = 74.3$. We can compare this value with the official analysis (blue) $\chi_{min}^2 = 99.3$, which corresponds to a p-value of 1.7×10^{-5} for 2 dof. Thus, our exclusion has a less restrictive high Δm^2 limit, coming mainly from including the energy miscalibration. At high Δm^2 , the upper limit should be driven by the flux normalization, which should dominate both the low and high energy samples, so it is unclear why the green (low-energy) and orange (high-energy) exclusions do not agree.

F. Updated for these fits: Reactors

The several inputs from reactor experiments have relatively modest updates compared to the 2019 fits

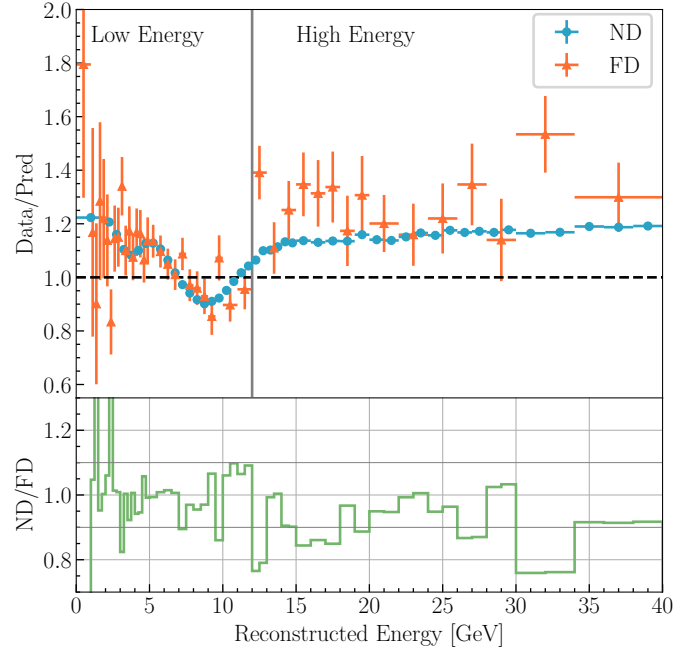


FIG. 6. Ratio between the data and the charge current MC prediction (top) for MINOS and MINOS+ for the near (blue) and far (orange) detector. For the prediction we have used $\Delta m_{41}^2 = 10^3 \text{ eV}^2$ and $\sin^2 \theta_{24} = 0.0025$. In the bottom panel, we show the ratio between the near and far detector predictions.

(Ref. [5]).

The NEOS experiment is composed of a single detector. In order to minimize systematic errors due to nuclear reactor models, they compare their data with a reference flux. At the time of the 2019 fits, NEOS used Daya Bay's unfolded $\bar{\nu}_e$ flux measurement [83]. Since then, the NEOS collaboration conducted a joint analysis with the RENO collaboration [84]. Now, the unfolded $\bar{\nu}_e$ flux measurement from the RENO near detector is used as the reference flux. The RENO near detector is placed at the same reactor complex as the NEOS detector, so this change reduces the systematic errors which may arise due to using different reactor cores. The NEOS detector data, otherwise, remains unchanged. We update the NEOS fits accordingly.

The PROSPECT data have been updated since the 2019 fit. The previous data set had a reactor-on time of 33 days [85], while the most recent data set has a reactor-time of 96 days [86].

A more important update is that STEREO [38] is now included in the global fits, which was not the case for the 2019 global fits because the data were not yet published. However, the 2019 global fits updated with STEREO appeared in Ref. [79]. The STEREO data are given in eleven energy bins across six different cells of increasing baseline, separated between two different run periods for a total of 179 days of reactor-on data. The fit

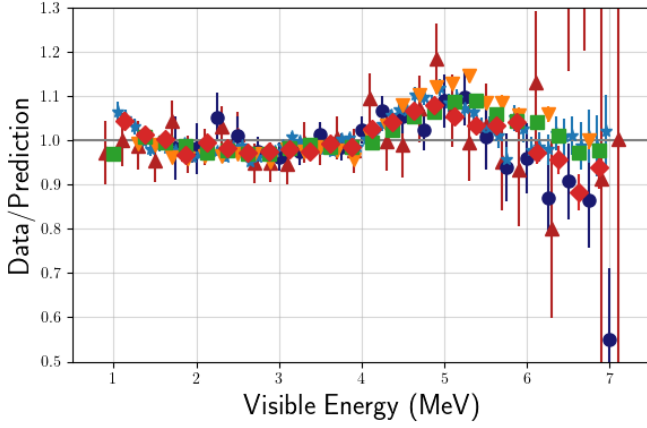


FIG. 7. Reactor data normalized by the predicted flux. Data are from RENO (inverted triangle) [87], Daya Bay (square) [88], Double Chooz (diamond) [89], NEOS (stars) [90], PROSPECT (triangle) [54] and STEREO (solid dots) [38].

incorporates free normalization parameters for each energy bin, thus remaining agnostic to the reactor $\bar{\nu}_e$ flux while searching for oscillations as a function of baseline. Following the recommendation of the STEREO collaboration [38], we impose a 20% uncertainty on the overall rate to compensate for the nonstandard $\Delta\chi^2$ distribution compared to the assumption from Wilks' theorem.

G. Comments about the Reactor Data

Overall, the reactor data sets deserve substantial discussion. These data sets exhibit structure that does not necessarily cancel in ratios and that may not be due to oscillations. The structure varies from experiment to experiment.

Let us begin by considering the measured reactor energy spectrum compared to the prediction. This is summarized for many reactor experiments, not all of which are used in these global fits because of their baseline length, in Fig. 7. One sees experiments running at power reactors (RENO, Daya Bay, Double Chooz, NEOS) and those running at research (LEU) reactors (PROSPECT, STEREO) have generally similar features. A well-known 5 MeV excess (often called a “bump”) is observed. What is not thoroughly discussed within the community is that other features also appear. There is a deficit in some experiments above 6 MeV. There is an excess in most experiments below 1.5 MeV. The range between 1.5 and 4 MeV may have structure also. While it is convenient to show many reactor data sets on one plot, additional individual spectral features are obscured.

The assumption has been that these features are due to unmodeled contributions to the reactor flux spectrum, in which case the features will have no L dependence. In response to this, reactor experiments

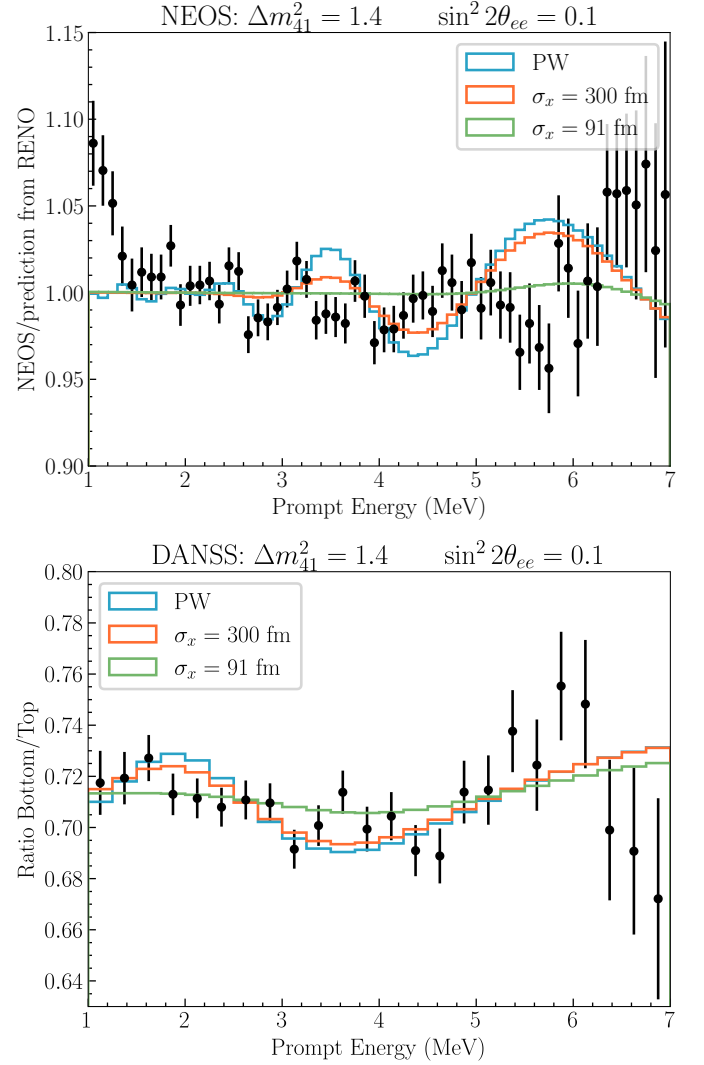


FIG. 8. The NEOS/RENO data ratio (top) and the DANSS data bottom/top ratio (bottom). Fits are to 3+1 and wave packet models discussed in sec. V

have switched to methods aimed at reducing sensitivity to non- L -dependent structure. Two approaches are shown in Fig. 8. The top plot attempts to remove non-oscillation structure in the NEOS [90] experiment data through normalizing to the RENO data from the same reactor complex [87]. The bottom plot presents data from DANSS, which moves the detector to regularly alternate data-taking at three locations from the reactor core, 10.7 m (top), 11.7 m, and 12.7 m (bottom). This case shows the bottom-to-top ratio [53]. In principle, all remaining structure should be due to L -dependent new physics effects.

Comparing the structure seen in DANSS and NEOS/RENO in Fig. 8 to the predictions of Fig. 1, one sees that the extreme wavepacket and decay scenarios have very similar features to the structure that remains in these plots. In Fig. 8, we present the 3+1 plane wave

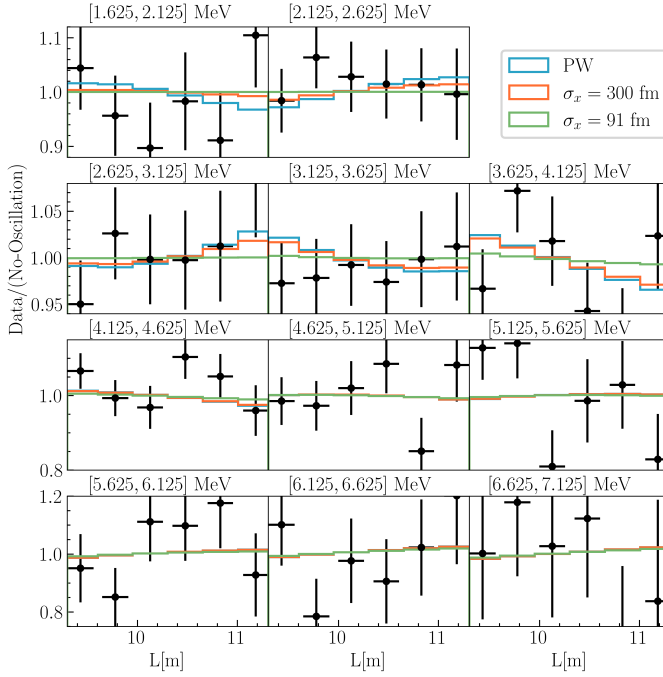


FIG. 9. The STEREO L dependence in each energy bin compared to the same models presented for NEOS/RENO and DANSS. Note the varying y -axis range.

(PW) and the two wave-packet examples considered earlier so that the effect is clear. One sees that our example damped scenarios will provide better fits to these data sets than the plane wave solution. It is also true for the 3+1+dk case. The concern is that, in practice, non-oscillation excess and deficits did not perfectly cancel due to systematic effects. Considering DANSS as an example, the peak at 6 MeV may be from imperfect cancellation of the 5 MeV bump leaving a tail. The dip at higher energy may be due to imperfect cancellation of the high energy dip seen in Fig. 7. It is difficult for those doing global fits to conjecture why there would not be full cancellation because we do not have hypotheses for the source of the underlying structure. Therefore, it is very important that those who perform the reactor experiments revisit the potential systematic uncertainties in the reactor fits to understand if this is signal or an uncharacterized background.

Regardless of unexpected energy dependence, if one considers the L dependence in each energy bin, then, in principle, an oscillation signature should be visible. The STEREO and PROSPECT data are treated in this manner, as per the recommendation of those collaborations. STEREO data, as seen in Fig. 9, are fit for the shape of the L dependence in individual energy bins, with the overall rate in each energy bin left as a free parameter. In the case of PROSPECT, the prediction at each baseline and energy is scaled according to the ratio of the total observed and predicted event rate across all baselines for each energy bin. Here, to illustrate this, in Fig. 10 we

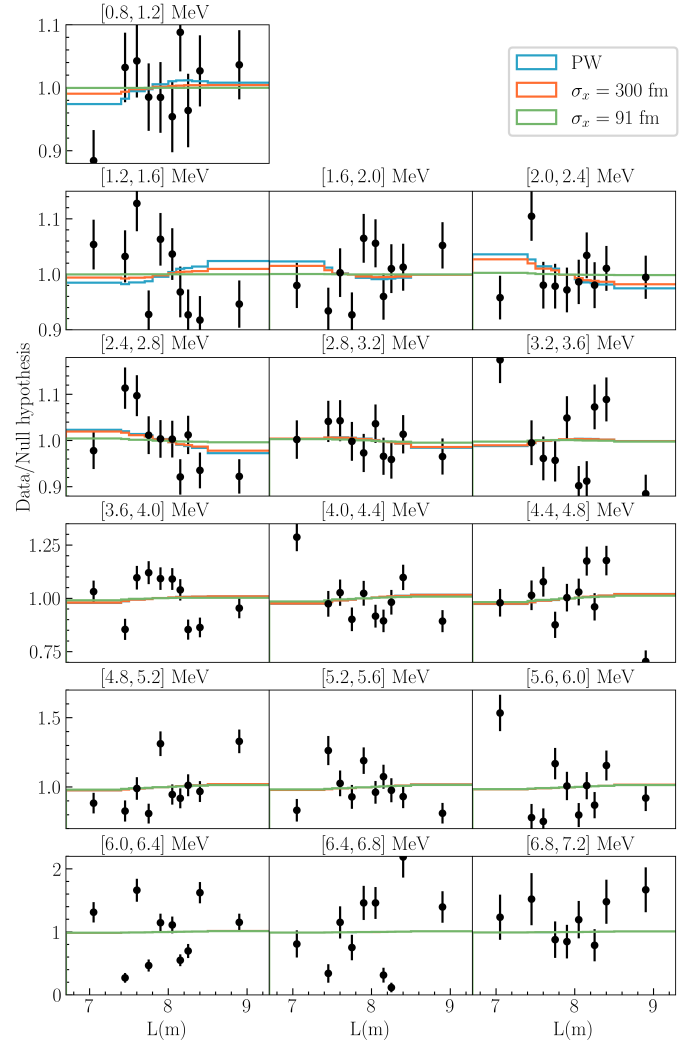


FIG. 10. PROSPECT L dependence in each energy bin compared to the same models presented for NEOS/RENO and DANSS. Note the varying y -axis range.

show the ratio of the data scaled to the prediction. In both cases, the effects we are considering in this discussion, indicated by the blue and orange lines, are small compared to the data uncertainty, and so these data are in agreement with the DANSS and NEOS/RENO conclusions.

IV. ABOUT THE FITTING CODE AND METHODS USED TO QUANTIFY RESULTS

The fitting code uses a Markov Chain Monte-Carlo (MCMC) as described in Ref. [5]. Each experiment is considered independently, but individual experimental systematics are included based on information from the relevant collaboration. The MCMC has the convenient property of sampling the model space, which allows us to use its sample points to display confidence regions and

exclusion curves. The confidence regions are described in two dimensions (Δm^2 and $\sin^2 2\theta$) using Wilks' theorem with 2 degrees of freedom on the profiled χ^2 , and this is what we report here. The Bayesian fits leverage the sampling nature of the MCMC and log-uniform priors to create dense Bayesian credible regions as described in Ref. [5]. We compare the Bayesian to the Wilks' theorem approach and find agreement, with more allowed space in the Bayesian case, but do not present those results here. A Wilks/Bayesian comparison can be found in Ref. [5].

Specifically, to quantify the quality of the fits, we use $\Delta\chi^2 = \chi_{null}^2 - \chi_{model}^2$ unless otherwise noted. The $\Delta\chi^2$ subtracts the contribution from bins irrelevant to the model.

The focus of concern over many years has been the compatibility of subsets of data within the overall collection of global data. For a detailed discussion see Ref. [5], but in particular, the appearance (app) (column 1 of Table I) and disappearance (dis) sets (columns 2 and 3 of Table I) when fit separately in a 3+1 model, show little overlap of preferred parameter space. The concern is that this points to different sources of anomalous effects in the two subsets, even in the presence of a large improvement in the global fit indicated by the $\Delta\chi^2$.

The agreement within subsets is traditionally measured through the parameter goodness of fit (PG) test [91]. Along with the global fit (glob), the two subsets are fit separately allowing one to form an effective χ^2 :

$$\chi_{PG}^2 = \chi_{glob}^2 - (\chi_{app}^2 + \chi_{dis}^2). \quad (11)$$

The number of degrees of freedom is then:

$$N_{PG} = (N_{app} + N_{dis}) - N_{glob}, \quad (12)$$

where each N is the number of independent parameters involved in the given fit. To be specific for a model important to this discussion, for the 3+1+WP case, global and dis will each have four parameters, Δm^2 , $|U_{e4}|^2$, $|U_{\mu4}|^2$ and σ_x , and app will have two parameters, Δm^2 and $|U_{e4}|^2|U_{\mu4}|^2$ since this case does not fit for σ_x , so $N_{PG} = (4 + 2) - 4 = 2$. In contrast, the example of the 3+1+dk case, where Γ is fit in all data subsets, $N_{PG} = (4 + 3) - 4 = 3$. The probability is based on a χ^2 distribution for χ_{PG}^2 and N_{PG} and is defined as the “tension” between the subsets.

V. RESULTS

It has been clear for many years that 3+1 is an inadequate model to explain the data. However, as we present results, we begin with this model for three reasons. First, it is widely used, even if known to be inadequate. Second, the features that appear are instructive. Third, the comparison to models with damping (3+1+WP and 3+1+dk) will highlight that those models are vastly better at describing the data. For completeness, we also include results from 3+2 and 3+3 to show that those

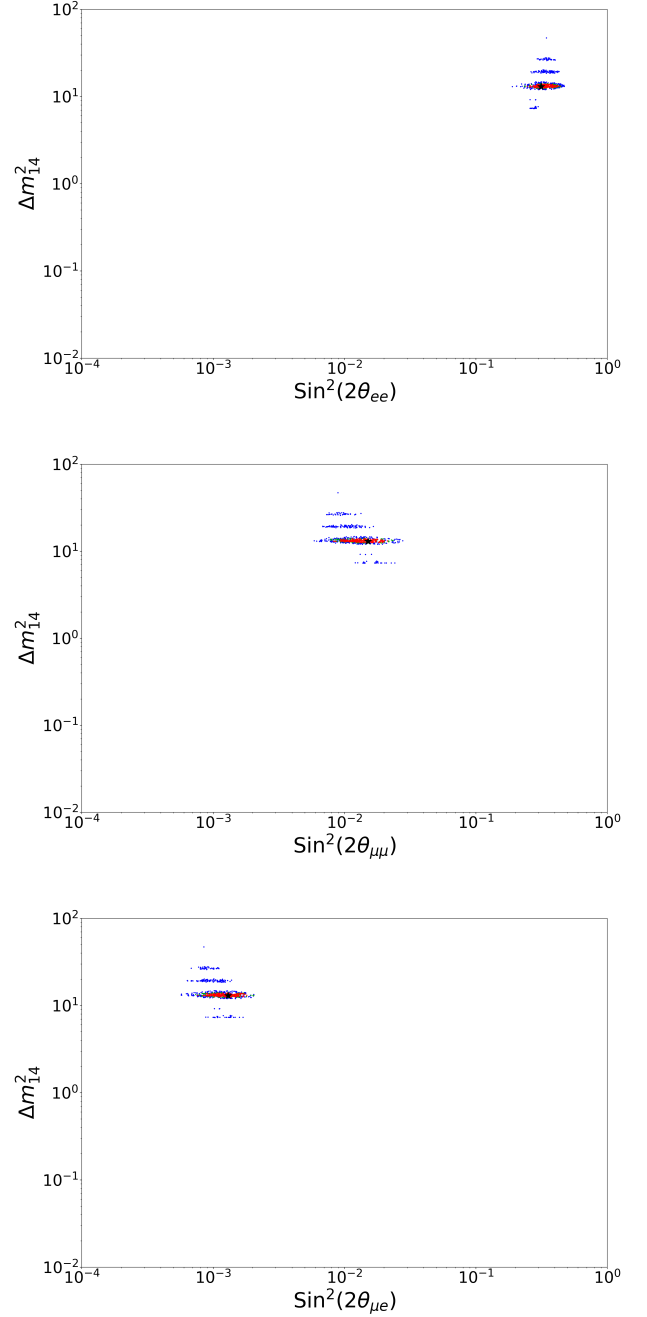


FIG. 11. The plane wave 3+1 fit results to the 2022 data sets. Top: ν_e disappearance; Middle: ν_μ disappearance; Bottom: appearance. Note that each plot is a projection profiled from the 3D fit space.

models result in less improvement. That points to a preference for less structure (damping) in the data than for more structure (many mass splittings). The results are summarized in Table II.

Fit type:	3+1	3+2	3+3	3+1+WP	3+1+dk
(Null vs Sterile)					
$\Delta\chi^2$	46.5	53.8	64.6	60.2	60.6
Δdof	3	7	12	4	4
p -value	4.4E-10	2.6E-09	3.2E-09	2.6E-12	2.2E-12
$N\sigma$	6.2	6.0	5.9	7.0	7.0
(3+1 vs Other)					
$\Delta\chi^2$		5.9*	16.7*	13.7	14.1
Δdof		4	9	1	1
p -value		0.21	0.054	2.1E-4	1.7E-4
$N\sigma$		1.3	1.9	3.7	3.8
(PG Test)					
χ_{app}^2	148.2	131.9	132.1	148.4	146.8
N_{app}	2	5	9	2	3
χ_{dis}^2	639.8	625.5	625.1	640	641.4
N_{dis}	3	6	9	4	4
χ_{glob}^2	816.1	799	788.5	802.4	807.5
N_{glob}	3	7	12	4	4
χ_{PG}^2	28.1	41.6	31.3	15.7	19.3
N_{PG}	2	4	6	2	3
p -value	7.9E-07	2.0E-08	2.2E-05	3.9E-04	2.4E-4
$N\sigma$	4.9	5.6	4.2	3.6	3.7

TABLE II. A summary of the quality of the fits. Columns correspond to the five types of fits. Top section: Comparison of quality of null to each fit including sterile neutrinos; Second section: Comparison of 3+1 to the extended models; Bottom section: PG test results for each model, where Eqs. 11 and 12 explain how χ_{PG}^2 and N_{PG} are determined. The asterisk (*) denotes that the 3+2 and 3+3 models are compared to a 3+1 fit that does not include IceCube, as explained in the text.

A. 3+1 (Plane Wave) Fit results

This section describes the 2022 results for fits to the commonly used, plane-wave 3+1 model. Results are shown in Fig. 11. One sees that the new fits prefer a $\Delta m^2 = 13 \text{ eV}^2$ compared to 1.3 eV^2 from the 2019 fits—an order of magnitude shift. This large shift is due to the interplay of the new inclusion of BEST, which has little L dependence, and so fits well at large Δm^2 but requires very large mixing, and the updated collection of reactor data that is poorly fit by a 3+1 model, but that does not produce a strong limit above $\Delta m^2 = 10 \text{ eV}^2$. This forces the fit point to just above the reactor limit in the ν_e disappearance samples, as can be inferred from Fig. 11, top, and the other samples can find solutions in the same range, making this the best-fit point. The best-fit mixing matrix parameters are $|U_{e4}|^2 = 8.5 \times 10^{-2}$ and $|U_{\mu 4}|^2 = 3.8 \times 10^{-3}$. The $\Delta\chi^2$ for 3+1 compared to the null is 46.5/3, which is an extraordinary improvement from adding one sterile neutrino—far more than 5σ . This says that some effect that is not in the null prediction and that has features similar to 3+1 is very strongly preferred by the data.

The range of axes in the plots of Fig. 11 shows the parameter space searched for this analysis. The plots in Fig. 11 are showing projections profiled from the 3D parameter space into the 2D planes. Although a large space is searched, the allowed regions are small. Since there is only one answer, that, in itself, is not an issue. While the regions are small, the best fit χ^2 minimum is very deep compared to null.

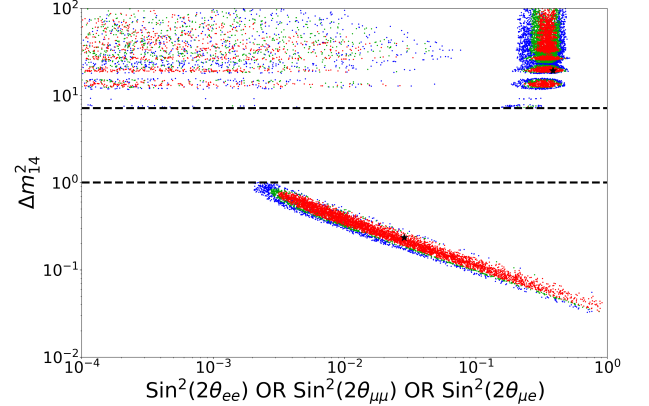


FIG. 12. Illustration of the tension within the 3+1 fit. Results of separate app and dis fits for the ν_μ disappearance (populating upper left), ν_e appearance (populating upper right), and appearance (populating lower region) data sets. The dashed lines guide the eye on the level of the gap in preferred Δm^2 .

With that said, there is well-known tension internal to the data sets that has become worse with these 2022 fits. In Fig. 12, we show the separate allowed regions for electron and muon disappearance (dis) and muon to electron appearance (app) overlaid on the same plot. The dis solution corresponds to ν_μ disappearance (upper left, low mixing angles) and ν_e disappearance (upper right, large mixing angles). Since $\sin^2 2\theta_{ee}$ and $\sin^2 2\theta_{\mu\mu}$ are

Fit	App vs. Dis tension	Δm^2 best fit (eV ²) App., Dis, Global
3+1	4.9σ	0.24, 7.8, 13
3+1+WP	3.5σ	0.24, 1.4, 1.4
3+1+WP, No MiniBooNE	2.8σ	0.85, 1.4, 1.4

TABLE III. Progression of reduction of tension of fits from 3+1 to 3+1+WP to 3+1+WP with MiniBooNE removed from fit.

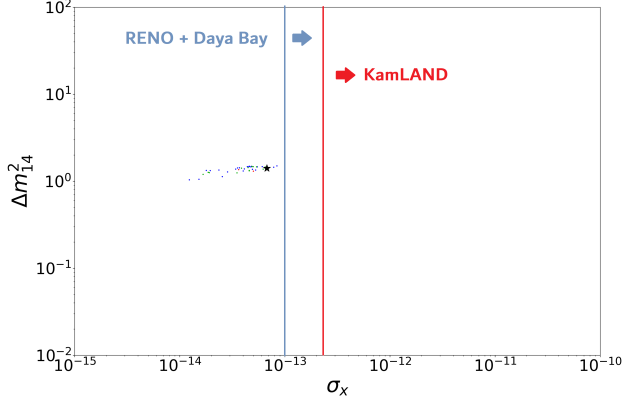


FIG. 13. The relationship between the fit mass splitting and the characteristic wavepacket size, σ_x , in the 3+1 global fit. The 90% limits set by RENO and Daya Bay are shown in blue with the limits from KamLAND shown in red. Limits are from [15]. Note that this plot is a projection profiled from the 4D fit-space.

independent, these two data sets are compatible with $\Delta m^2 = 7.8 \text{ eV}^2$. However, there is a large gap in Δm^2 between the disappearance and the appearance data set preferred fit regions (dashed lines), and the appearance preferred fit is at 0.24 eV^2 . From this plot, one can see that the tension between the app and dis will be very high, and that the global fit Δm^2 at 13 eV^2 is a disagreeable compromise for both. Making this quantitative using the PG test discussed in Sec. IV, the level of disagreement is $\chi^2_{PG}/N_{PG} = 28.1/2$, which represents a 4.9σ tension, in qualitative agreement with prior work and the literature.

B. 3+1+WP Fit Results

Introducing 3+1+WP leads to a substantial improvement in the fit results. We have qualitatively discussed the reason for this in Sec. III G. Here, we discuss the quantitative results.

The improvement in the fit compared to the null is $\Delta\chi^2/\text{dof} = 60.2/4$, and is $13.7/1$ compared to 3+1. The best-fit $\Delta m^2 = 1.4 \text{ eV}^2$ which is in excellent agreement with the 2019 fit. The best-fit mixing matrix parameters are $|U_{e4}|^2 = 9.5 \times 10^{-2}$ and $|U_{\mu 4}|^2 = 2.9 \times 10^{-3}$. Plots of

the allowed regions are provided in Appendix A. For the wavepacket size, the best fit finds $\sigma_x = 67 \text{ fm}$. This can be compared to the reactor data fit alone, which prefers 91 fm corresponding to the green curve on Fig. 1, or $> 20 \text{ fm}$ at 99% CL, hence is in agreement. Thus, this model is introducing strong damping on the reactor prediction at low energy but the best fit allows shape effects at large energies.

Fig. 13 shows the wavepacket fit as a function of Δm^2 , and it should be noted that the resulting fit is bounded at low and high σ_x , so this is not a limit, it is a measurement. This point is within $< 2\sigma$ of the fit in Ref. [16] which fit for σ_x using Daya Bay and RENO. We note that our fits do not use Daya Bay, so the only overlap is through RENO which is used to normalize the NEOS result. Our fit includes many other reactor experiments (see Table I, column 1, row 2), so our takeaway is that relatively short baseline experiments ($L \lesssim 1 \text{ km}$) are providing consistent information with the longer RENO and Daya Bay baselines. With that said, when KamLAND is added to the RENO+Daya Bay fit in Ref. [15] is inconsistent. So there is complexity in understanding the meaning of this parameter.

The 3+1+WP model has substantially less tension compared to null when comparing app versus dis than 3+1. The χ^2_{PG}/N_{PG} for this model is $15.7/2$. This represents 3.5σ which is still significant but is substantially better than the 4.9σ of the 3+1 case. Subtracting these in quadrature, the 3.4σ level reduction indicates that the data has significantly less tension. Another way to say this is that the χ^2_{PG} improved by 12.4 units with the addition of only 1 additional degree of freedom. Fig. 14, top, allows one to visualize the improvement. The gap between the allowed regions for dis and app has been greatly reduced compared to Fig. 12.

Of the remaining tension within the model, the bulk comes from MiniBooNE, which has been observed to be consistent with ν_e CCQE-like scattering with some additional contribution. To show this, we consider fits with and without the MiniBooNE data. The progression of improvement in tension is presented in Table III, and is also illustrated by the overlap of the app and dis data sets in Fig. 14, bottom, which shows the allowed regions with MiniBooNE removed. One sees that MiniBooNE is contributing 2.1σ of tension, which can be compared to the 3.4σ relief of tension that comes from including damping for reactors. This leaves 2.7σ of tension that is yet to be understood, and that appears to come from a combination of relatively small effects in the remaining data sets that combine to add overall tension to the fit.

C. 3+1+dk Fit Results

The 3+1+dk model yields a similar result to 3+1+WP, underlining the preference for a damping term. The best fit is $\Delta m^2 = 1.4 \text{ eV}^2$; the best-fit mixing parameters are $|U_{e4}|^2 = 1.0 \times 10^{-1}$ and $|U_{\mu 4}|^2 = 5.5 \times 10^{-3}$; and

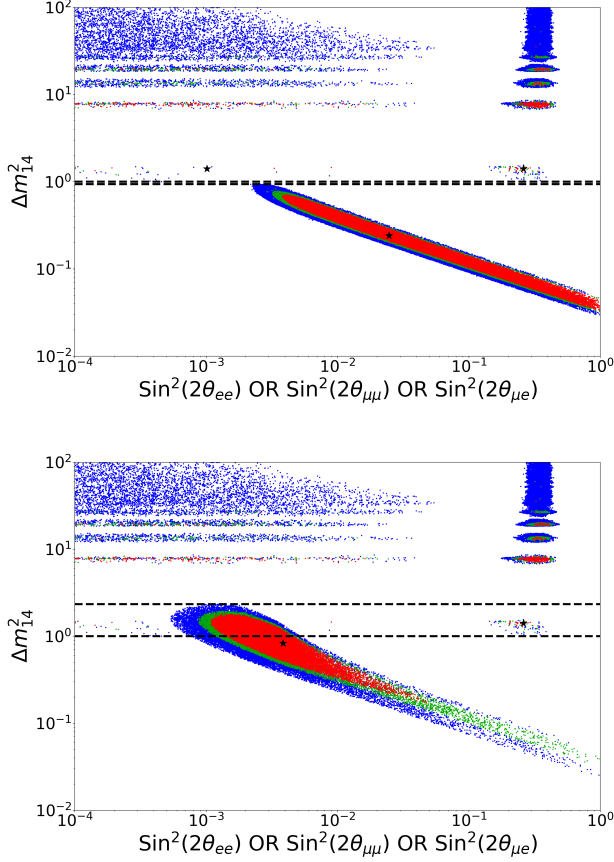


FIG. 14. Top: Illustration of the tension within the fit. The gap between the dis and app allowed regions is greatly reduced. Bottom: Same but with the MiniBooNE appearance data set removed from the fits. At this point, one sees overlap of the 2σ regions between the app and dis allowed regions.

the best-fit $\Gamma = 0.35$ eV. The example given in green in Fig. 1, bottom is from the reactor only fit at a similar value of $\Gamma = 0.29$ eV. Plots of the allowed regions are provided in Appendix B. The difference between the models is that in this case the damping parameter affects all data sets rather than just the reactor experiments and has a slightly different dependence on L/E . The overall goodness of fit matches 3+1+WP, with $\Delta\chi^2$ compared to 3+1 of 14.1 for only 1 additional fit parameter. The tension in this model is compared to 3+1 and 3+1+WP in Table II. For this model, when fitting all experiments, the χ^2_{PG} is 19.3 for $N_{PG} = 3$, hence the tension is at the 3.7σ level. One can gain a visual sense of the relative improvement by comparing Fig. 15 to Figs. 12 and 14, top. One sees that while there are differences in the allowed regions overall, 3+1+WP and 3+1+dk are improving the fits overall.

As a similar test to the wavepacket case, we have fit the reactor experiments separately. We find $\Gamma = 0.29$ eV, which is very similar to the $\Gamma = 0.35$ eV case for the for the global fit. These are both also similar to the

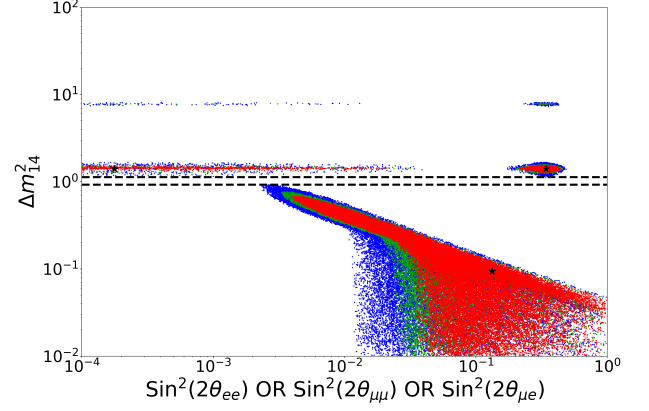


FIG. 15. Illustration of the tension within the 3+1+dk fit. The gap between the dis and app allowed regions is greatly reduced compared to 3+1 (Fig. 12), but not to the level of 3+1+WP (14 top).

IceCube-only best fit point, which is $\Gamma = 0.40$. Thus, this parameter appears to be consistent across data sets.

D. 3+2 and 3+3 fit Results

One can question whether the improvement comes specifically from damping or from adding extra degrees of freedom in general. Two often-tested models with substantially higher degrees of freedom are 3+2 and 3+3 models, with 7 and 12 parameters, respectively. Unlike adding a damping term, these models add additional mass splittings that produce interference effects, allowing very complex waves to be fit to the global data.

The tension results are reported in Table II, where the asterisk (*) denotes that these fits do not include IceCube. IceCube cannot be included in these fits because the necessary likelihood information is not released. Therefore, when we fit a separate set of 3+1 data without IceCube for comparison. The overall $\Delta\chi^2/\text{dof}$ measured with respect to the null is 799 (788.5)/ 7 (12) for 3+2 (3+3). For the record, the parameters from the 3+2 fit are: the 2 mass splittings 4 mixing elements ($U_{\alpha i}$), and 1 CP violating phase. For the 3+3 fit, they are: The 3 mass splittings 6 mixing elements ($U_{\alpha i}$), and 3 CP violating phases. A table the parameters appears in Appendix C.

It is striking to note that the 3+2 tension is 2.7σ larger in these fits than for the 3+1 that includes IceCube when one would expect that adding additional parameters would relieve tension. This shows that the IceCube data is playing an important role and we encourage IceCube to pursue at least the 3+2 fits, recognizing that 3+3 fits may be computationally prohibitive.

VI. DISCUSSION AND CONCLUSION

We have performed global fits to the 2022 short-baseline vacuum-oscillation data sets and the ν_μ matter-resonance data from IceCube. The data show a strong preference for a 3+1+WP model or for a 3+1+dk model. These models have the effect of damping oscillations at low energy in the reactor data. However, some modulation is preferred at high energies. These models, which each introduce one new parameter, are essentially indistinguishable in their major improvement to the fits. On the other hand, models that introduce additional parameters but do not involve damping effects, such as 3+2 and 3+3, are less successful at relieving tension.

These studies show that a large fraction of the internal tension from 3+1 fits comes from the reactors, a point that has not previously been noted. However, when the damped models are employed some tension remains. The remaining tension is greatly improved when MiniBooNE is not included in the fit. This indicates some fraction of the MiniBooNE excess events are inconsistent with the global picture of oscillations, a point that has been noted previously.

Lastly, we point out that the reactor event spectrum has a great deal more structure beyond the 5 MeV excess that is typically discussed. Reactor experiments have taken steps in analyzing data to reduce sensitivity to the unexplained structure. However, it is not clear that the techniques employed fully remove residual, L -dependent effects. As a result, we urge the reactor community to revisit the systematic errors. Results that set limits receive less scrutiny than results that indicate signals, and this might have led to systematic effects being overlooked. However, it is crucial that this question be revisited because, if systematic effects have not been overlooked, then the structure in reactor experiments is pointing toward new physics that damps 3+1 oscillations.

VII. ACKNOWLEDGEMENTS

MHS is supported by NSF grant PHY-1707971 and NSF grant PHY-1912764 supported JMC, AD, and JMH. NWK is also supported by the NSF Graduate Research Fellowship under Grant No. 1745302. CAA, IMS, and MJ are supported by the Faculty of Arts and Sciences of Harvard University. Additionally, CAA and IMS are supported by the Alfred P. Sloan Foundation.

-
- [1] I. Esteban, M. Gonzalez-Garcia, M. Maltoni, T. Schwetz, and A. Zhou, *Journal of High Energy Physics* **2020** (2020), URL <https://doi.org/10.1007/2Fjhep09%282020%29178>.
 - [2] R. L. Workman and Others (Particle Data Group), *PTEP* **2022**, 083C01 (2022).
 - [3] J. Kopp, P. A. N. Machado, M. Maltoni, and T. Schwetz, *JHEP* **05**, 050 (2013), 1303.3011.
 - [4] S. Gariazzo, C. Giunti, M. Laveder, and Y. F. Li, *JHEP* **06**, 135 (2017), 1703.00860.
 - [5] A. Diaz, C. Argüelles, G. Collin, J. Conrad, and M. Shaevitz, *Phys. Rept.* **884**, 1 (2020), 1906.00045.
 - [6] M. A. Acero et al. (2022), 2203.07323.
 - [7] C. A. Argüelles, T. Bertólez-Martínez, and J. Salvado (2022), 2201.05108.
 - [8] S. Palomares-Ruiz, S. Pascoli, and T. Schwetz, *JHEP* **09**, 048 (2005), hep-ph/0505216.
 - [9] Z. Moss, M. H. Moulai, C. A. Argüelles, and J. M. Conrad, *Phys. Rev. D* **97**, 055017 (2018), 1711.05921.
 - [10] G. Collin, C. Argüelles, J. Conrad, and M. Shaevitz, *Phys. Rev. Lett.* **117**, 221801 (2016), 1607.00011.
 - [11] J. Conrad, C. Ignarra, G. Karagiorgi, M. Shaevitz, and J. Spitz, *Adv. High Energy Phys.* **2013**, 163897 (2013), 1207.4765.
 - [12] M. Sorel, J. M. Conrad, and M. Shaevitz, *Phys. Rev. D* **70**, 073004 (2004), hep-ph/0305255.
 - [13] M. H. Moulai, C. A. Argüelles, G. H. Collin, J. M. Conrad, A. Diaz, and M. H. Shaevitz, *Phys. Rev. D* **101**, 055020 (2020), 1910.13456.
 - [14] N. M. Coyle, S. W. Li, and P. A. N. Machado (2022), 2210.03753.
 - [15] A. de Gouvêa, V. De Romeri, and C. A. Ternes, *JHEP* **06**, 042 (2021), 2104.05806.
 - [16] A. de Gouvea, V. de Romeri, and C. A. Ternes, *JHEP* **08**, 018 (2020), 2005.03022.
 - [17] E. Marzec and J. Spitz, *Phys. Rev. D* **106**, 053007 (2022), 2208.04277.
 - [18] E. Akhmedov and A. Y. Smirnov (2022), 2208.03736.
 - [19] B. J. P. Jones (2022), 2209.00561.
 - [20] E. Akhmedov and A. Y. Smirnov (2022), 2210.01547.
 - [21] B. Jones, E. Marzec, and J. Spitz (2022), 2211.00026.
 - [22] H. Banks, K. J. Kelly, and M. McCullough (2022), 2209.11270.
 - [23] E. Ma and G. Rajasekaran, *Phys. Rev. D* **64**, 117303 (2001), hep-ph/0107203.
 - [24] S. Palomares-Ruiz, S. Pascoli, and T. Schwetz, *JHEP* **09**, 048 (2005), hep-ph/0505216.
 - [25] S. Gninenko, *Phys. Rev. Lett.* **103**, 241802 (2009), 0902.3802.
 - [26] C. Dib, J. C. Helo, S. Kovalenko, and I. Schmidt, *Phys. Rev. D* **84**, 071301 (2011), 1105.4664.
 - [27] M. Masip, P. Masjuan, and D. Meloni, *JHEP* **01**, 106 (2013), 1210.1519.
 - [28] M. Masip and P. Masjuan, *Phys. Rev. D* **83**, 091301 (2011), 1103.0689.
 - [29] S. Gninenko, *Phys. Lett. B* **710**, 86 (2012), 1201.5194.
 - [30] P. Ballett, S. Pascoli, and M. Ross-Lonergan, *Phys. Rev. D* **99**, 071701 (2019), 1808.02915.
 - [31] P. Ballett, S. Pascoli, and M. Ross-Lonergan, *JHEP* **04**, 102 (2017), 1610.08512.
 - [32] O. Fischer, A. Hernández-Cabezudo, and T. Schwetz, *Phys. Rev. D* **101**, 075045 (2020), 1909.09561.

- [33] M. Dentler, I. Esteban, J. Kopp, and P. Machado, Phys. Rev. D **101**, 115013 (2020), 1911.01427.
- [34] A. de Gouvêa, O. Peres, S. Prakash, and G. Stenico, JHEP **07**, 141 (2020), 1911.01447.
- [35] A. de Gouvea, P. J. Fox, B. J. Kayser, and K. J. Kelly (2021), 2104.05719.
- [36] R. Abbasi, M. Ackermann, J. Adams, J. A. Aguilar, M. Ahlers, M. Ahrens, J. M. Alameddine, A. A. Alves, N. M. Amin, K. Andeen, et al. (IceCube Collaboration), Phys. Rev. Lett. **129**, 151801 (2022), URL <https://link.aps.org/doi/10.1103/PhysRevLett.129.151801>.
- [37] V. V. Barinov et al. (2022), 2201.07364.
- [38] H. Almazán, L. Bernard, A. Blanchet, A. Bonhomme, C. Buck, P. del Amo Sanchez, I. El Atmani, J. Haser, F. Kandzia, S. Kox, et al. (STEREO Collaboration), Phys. Rev. D **102**, 052002 (2020), URL <https://link.aps.org/doi/10.1103/PhysRevD.102.052002>.
- [39] P. Abratenko et al. (MicroBooNE) (2021), 2110.13978.
- [40] A. A. Aguilar-Arevalo et al. (MiniBooNE) (2022), 2201.01724.
- [41] D. G. Michael et al. (MINOS), Nucl. Instrum. Meth. A **596**, 190 (2008), 0805.3170.
- [42] M. Aartsen et al. (IceCube), Phys. Rev. Lett. **125**, 141801 (2020), 2005.12942.
- [43] A. A. Aguilar-Arevalo et al. (MiniBooNE), Phys. Rev. Lett. **110**, 161801 (2013), 1303.2588.
- [44] P. Adamson et al. (MiniBooNE, MINOS), Phys. Rev. Lett. **102**, 211801 (2009), 0809.2447.
- [45] P. Astier et al. (NOMAD), Phys. Lett. **B570**, 19 (2003), hep-ex/0306037.
- [46] A. Aguilar-Arevalo et al. (LSND), Phys. Rev. D **64**, 112007 (2001), hep-ex/0104049.
- [47] B. Armbruster et al. (KARMEN), Phys. Rev. **D65**, 112001 (2002), hep-ex/0203021.
- [48] K. B. M. Mahn et al. (SciBooNE, MiniBooNE), Phys. Rev. **D85**, 032007 (2012), 1106.5685.
- [49] G. Cheng et al. (MiniBooNE, SciBooNE), Phys. Rev. **D86**, 052009 (2012), 1208.0322.
- [50] J. N. Abdurashitov et al. (SAGE), Phys. Rev. **C80**, 015807 (2009), 0901.2200.
- [51] F. Kaether, W. Hampel, G. Heusser, J. Kiko, and T. Kirsten, Phys. Lett. **B685**, 47 (2010), 1001.2731.
- [52] Y. Declais et al., Nucl. Phys. **B434**, 503 (1995).
- [53] I. Alekseev et al. (DANSS), Phys. Lett. **B787**, 56 (2018), 1804.04046.
- [54] M. Andriamirado, A. B. Balantekin, H. R. Band, C. D. Bass, D. E. Bergeron, D. Berish, N. S. Bowden, J. P. Brodsky, C. D. Bryan, T. Classen, et al. (PROSPECT Collaboration), Phys. Rev. D **103**, 032001 (2021), URL <https://link.aps.org/doi/10.1103/PhysRevD.103.032001>.
- [55] A. P. Serebrov et al., Phys. Rev. D **104**, 032003 (2021), 2005.05301.
- [56] C. Giunti, Y. F. Li, C. A. Ternes, and Y. Y. Zhang, Phys. Lett. **B 816**, 136214 (2021), 2101.06785.
- [57] P. B. Denton, Phys. Rev. Lett. **129**, 061801 (2022), 2111.05793.
- [58] C. A. Argüelles, I. Esteban, M. Hostert, K. J. Kelly, J. Kopp, P. A. N. Machado, I. Martinez-Soler, and Y. F. Perez-Gonzalez, Phys. Rev. Lett. **128**, 241802 (2022), 2111.10359.
- [59] P. Abratenko et al. (MicroBooNE) (2022), 2210.10216.
- [60] MicroBooNE Collaboration, *Search for an anomalous excess of inclusive charged-current ν_e interactions in the MicroBooNE experiment using Wire-Cell reconstruction*, HEPData (collection) (2022), <https://doi.org/10.17182/hepdata.114862>.
- [61] X. Ji, W. Gu, X. Qian, H. Wei, and C. Zhang, Nucl. Instrum. Meth. A **961**, 163677 (2020), 1903.07185.
- [62] R. J. Barlow and C. Beeston, Comput. Phys. Commun. **77**, 219 (1993).
- [63] D. Chirkin (2013), 1304.0735.
- [64] T. Glüsenskamp, Eur. Phys. J. Plus **133**, 218 (2018), 1712.01293.
- [65] C. A. Argüelles, A. Schneider, and T. Yuan, JHEP **06**, 030 (2019), 1901.04645.
- [66] T. Glüsenskamp, JINST **15**, P01035 (2020), 1902.08831.
- [67] P. Abratenko et al. (MicroBooNE), Phys. Rev. D **106**, L051102 (2022), 2208.02348.
- [68] V. V. Barinov et al., Phys. Rev. Lett. **128**, 232501 (2022), 2109.11482.
- [69] A. Diaz, Other thesis (2022), 2210.09418.
- [70] M. Dentler, A. Hernández-Cabezudo, J. Kopp, P. A. N. Machado, M. Maltoni, I. Martinez-Soler, and T. Schwetz, JHEP **08**, 010 (2018), 1803.10661.
- [71] M. G. Aartsen et al. (IceCube), Phys. Rev. Lett. **125**, 141801 (2020), 2005.12942.
- [72] R. Abbasi et al. ((IceCube Collaboration)*, IceCube), Phys. Rev. Lett. **129**, 151801 (2022), 2204.00612.
- [73] M. G. Aartsen et al. (IceCube), Phys. Rev. D **102**, 052009 (2020), 2005.12943.
- [74] M. H. Moulai, Ph.D. thesis, MIT (2021), 2110.02351.
- [75] M. G. Aartsen et al. (IceCube), JCAP **10**, 048 (2019), 1909.01530.
- [76] A. A. Aguilar-Arevalo et al. (MiniBooNE), Phys. Rev. D **103**, 052002 (2021), 2006.16883.
- [77] V. Brdar and J. Kopp, Phys. Rev. D **105**, 115024 (2022), 2109.08157.
- [78] K. J. Kelly and J. Kopp (2022), 2210.08021.
- [79] S. Vergani, N. W. Kamp, A. Diaz, C. A. Argüelles, J. M. Conrad, M. H. Shaevitz, and M. A. Uchida, PoS **NuFact2021**, 199 (2022).
- [80] N. W. Kamp, M. Hostert, A. Schneider, S. Vergani, C. A. Argüelles, J. M. Conrad, M. H. Shaevitz, and M. A. Uchida (2022), 2206.07100.
- [81] P. Adamson et al. (MINOS), Phys. Rev. Lett. **112**, 191801 (2014), 1403.0867.
- [82] P. Adamson et al. (MINOS+), Phys. Rev. Lett. **122**, 091803 (2019), 1710.06488.
- [83] Y. J. Ko et al. (NEOS), Phys. Rev. Lett. **118**, 121802 (2017), 1610.05134.
- [84] Z. Atif et al. (RENO, NEOS) (2020), 2011.00896.
- [85] J. Ashenfelter et al. (PROSPECT), Phys. Rev. Lett. **121**, 251802 (2018), 1806.02784.
- [86] M. Andriamirado et al. (PROSPECT), Phys. Rev. D **103**, 032001 (2021), 2006.11210.
- [87] J. H. Choi et al. (RENO), Phys. Rev. Lett. **116**, 211801 (2016), 1511.05849.
- [88] F. P. An et al. (Daya Bay), Chin. Phys. C **41**, 013002 (2017), 1607.05378.
- [89] Y. Abe et al. (Double Chooz), JHEP **01**, 163 (2016), 1510.08937.
- [90] Y. J. Ko et al. (NEOS), Phys. Rev. Lett. **118**, 121802 (2017), 1610.05134.
- [91] M. Maltoni and T. Schwetz, Phys. Rev. D **68**, 033020 (2003), hep-ph/0304176.

Appendix A: More information on Fit Parameter for 3+1+WP

For 3+1+WP, the projection profiled over the 4D parameters space for the three mixing angles is presented in Fig. 16. The limits of the plots indicate the range of parameters explored in these fits.

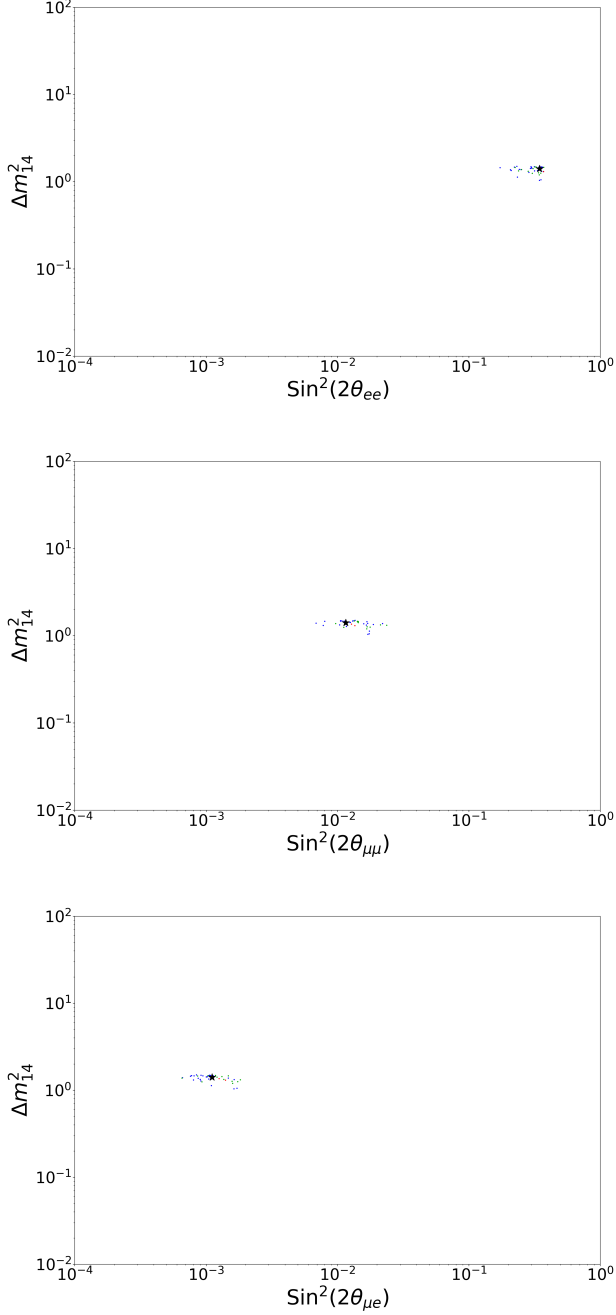


FIG. 16. The 3+1+WP mixing angle and mass splitting space. Top: ν_e disappearance; Middle: ν_μ disappearance; Bottom: appearance.

Appendix B: More information on Fit Parameters for 3+1+dk

For 3+1+dk, the projection profiled over the 4D parameters space for the mixing angles and the mass splitting are presented in Fig. 17. The decay width parameter space is explored in Fig. 18.

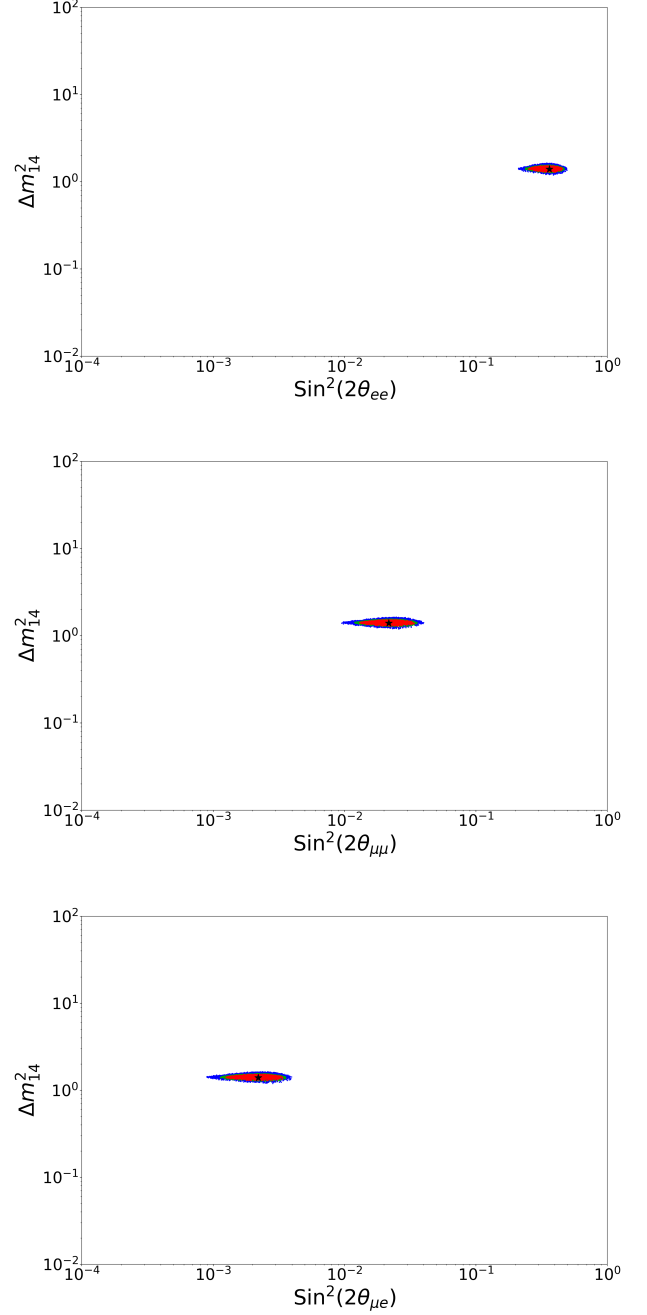


FIG. 17. The 3+1+dk mixing angle and mass splitting space. Top: ν_e disappearance; Middle: ν_μ disappearance; Bottom: appearance.

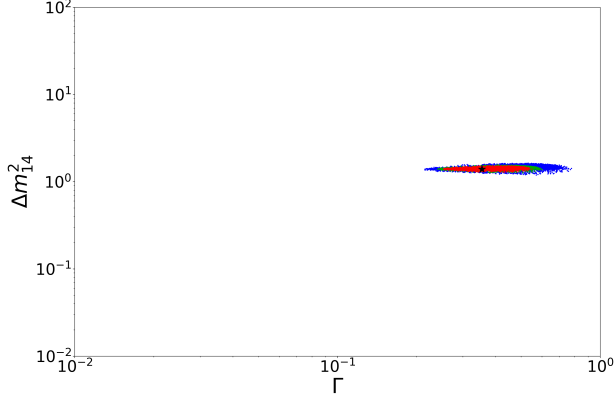


FIG. 18. The 3+1+dk Γ and mass splitting space.

Appendix C: Fit Parameters for 3+2 and 3+3

Table IV lists the best fit parameters for the 3+2 (top) and 3+3 (bottom) fits.

3+2	
$\Delta m_{41}^2, \Delta m_{54}^2$ in eV^2	3.4E+1, 3.5E+1
$U_{e4}, U_{\mu 4}$	2.7E-1, 6.5E-1
$U_{e5}, U_{\mu 5}$	1.5E-1, 1.3E-1
ϕ_{54}	3.0E+0
3+3	
$\Delta m_{41}^2, \Delta m_{54}^2, \Delta m_{65}^2$ in eV^2	7.2E-2, 2.1E-1, 1.9E+1
$U_{e4}, U_{\mu 4}$	6.0E-1, 7.2E-3
$U_{e5}, U_{\mu 5}$	8.4E-2, 9.9E-1
$U_{e6}, U_{\mu 6}$	3.0E-1, 4.2E-2
$\phi_{54}, \phi_{65}, \phi_{64}$	1.8E+0, 2.6E+0, 5.1E+0

TABLE IV. Best fit parameters for 3+2 (top) and 3+3 (bottom).